Low-pT direct-photon production in Au+Au collisions at √sNN=39 and 62.4 GeV

(PHENIX Collaboration) Abdulameer, N. J.; Acharya, U.; Adare, A.; Aidala, C.; Ajitanand, N. N.; Akiba, Y.; Akimoto, R.; Al-Ta'ani, H.; Alexander, J.; Alfred, M.; ...

Editors' Suggestion

Low-p_T direct-photon production in Au + Au collisions at $\sqrt{s_{NN}} = 39$ and 62.4 GeV

N. J. Abdulameer,[15] U. Acharya,[20] A. Adare,[11] C. Aidala,[39,45] N. N. Ajitanand,[66,*] Y. Akiba,[60,61,†] R. Akimoto,[10] H. Al-Ta'ani,[53] J. Alexander,[66] M. Alfred,[23] A. Angerami,[12] K. Aoki,[32,60] N. Apadula,[28,67] Y. Aramaki,[10,60] H. Asano,[35,60] E. C. Aschenauer,[7] E. T. Atomssa,[67] T. C. Awes,[56] B. Azmoun,[7] V. Babintsev,[24] M. Bai,[6] B. Bannier,[67] K. N. Barish,[8] B. Bassalleck,[52] S. Bathe,[5,61] V. Baublis,[58] S. Baumgart,[60] A. Bazilevsky,[7] R. Belmont,[11,54,73] A. Berdnikov,[63] Y. Berdnikov,[63] L. Bichon,[73] B. Blankenship,[73] D. S. Blau,[34,51] J. S. Bok,[52,53,76] V. Borisov,[63] K. Boyle,[61] M. L. Brooks,[39] H. Buesching,[7] V. Bumazhnov,[24] S. Butsyk,[52] S. Campbell,[12,67] V. Canoa Roman,[67] P. Castera,[67] C.-H. Chen,[61,67] M. Chiu,[7] C. Y. Chi,[12] I. J. Choi,[25] J. B. Choi,[30,*] S. Choi,[65] R. K. Choudhury,[4] P. Christiansen,[41] T. Chujo,[72] O. Chvala,[8] V. Cianciolo,[56] Z. Citron,[67,74] B. A. Cole,[12] M. Connors,[20,67] R. Corliss,[67] Y. Corrales Morales,[39] M. Csanád,[16] T. Csörgő,[44,75] L. D'Orazio,[42] S. Dairaku,[35,60] A. Datta,[43] M. S. Daugherity,[1] G. David,[7,67] C. T. Dean,[39] A. Denisov,[24] A. Deshpande,[61,67] E. J. Desmond,[7] K. V. Dharmawardane,[53] O. Dietzsch,[64] L. Ding,[28] A. Dion,[28,67] M. Donadelli,[64] V. Doomra,[67] O. Drapier,[36] A. Drees,[67] K. A. Drees,[6] J. M. Durham,[39,67] A. Durum,[24] S. Edwards,[6] Y. V. Efremenko,[56] T. Engelmore,[12] A. Enokizono,[56,60,62] R. Esha,[67] K. O. Eyser,[7,8] B. Fadem,[47] W. Fan,[67] D. E. Fields,[52] M. Finger, Jr.,[9] M. Finger,[9] D. Firak,[15,67] D. Fitzgerald,[45] F. Fleuret,[36] S. L. Fokin,[34] J. E. Frantz,[55] A. Franz,[7] A. D. Frawley,[19] Y. Fukao,[60] T. Fusayasu,[49] K. Gainey,[1] C. Gal,[67] A. Garishvili,[69] I. Garishvili,[38] M. Giles,[67] A. Glenn,[38] X. Gong,[66] M. Gonin,[36] Y. Goto,[60,61] R. Granier de Cassagnac,[36] N. Grau,[2] S. V. Greene,[73] M. Grosse Perdekamp,[25] T. Gunji,[10] L. Guo,[39] H.-Å. Gustafsson,[41,*] T. Hachiya,[50,60,61] J. S. Haggerty,[7] K. I. Hahn,[17] H. Hamagaki,[10] J. Hanks,[12,67] M. Harvey,[70] S. Hasegawa,[29] K. Hashimoto,[60,62] E. Haslum,[41] R. Hayano,[10] T. K. Hemmick,[67] T. Hester,[8] X. He,[20] J. C. Hill,[28] A. Hodges,[20] R. S. Hollis,[8] K. Homma,[22] B. Hong,[33] T. Horaguchi,[72] Y. Hori,[10] J. Huang,[7] T. Ichihara,[60,61] H. Iinuma,[32] Y. Ikeda,[60,72] J. Imrek,[15] M. Inaba,[72] A. Iordanova,[8] D. Isenhower,[1] M. Issah,[73] D. Ivanishchev,[58] B. V. Jacak,[67] M. Javani,[20] X. Jiang,[39] Z. Ji,[67] B. M. Johnson,[7,20] K. S. Joo,[48] D. Jouan,[57] D. S. Jumper,[25] J. Kamin,[67] S. Kaneti,[67] B. H. Kang,[21] J. H. Kang,[76] J. S. Kang,[21] J. Kapustinsky,[39] K. Karatsu,[35,60] M. Kasai,[60,62] D. Kawall,[43,61] A. V. Kazantsev,[34] T. Kempel,[28] V. Khachatryan,[67] A. Khanzadeev,[58] A. Khatiwada,[39] K. M. Kijima,[22] B. I. Kim,[33] C. Kim,[33] D. J. Kim,[31] E.-J. Kim,[30] H. J. Kim,[76] K.-B. Kim,[30] T. Kim,[17] Y.-J. Kim,[25] Y. K. Kim,[21] D. Kincses,[16] A. Kingan,[67] E. Kinney,[11] Á. Kiss,[16] E. Kistenev,[7] J. Klatsky,[19] D. Kleinjan,[8] P. Kline,[67] Y. Komatsu,[10,32] B. Komkov,[58] J. Koster,[25] D. Kotchetkov,[55] D. Kotov,[58,63] L. Kovacs,[16] F. Krizek,[31] A. Král,[13] G. J. Kunde,[39] B. Kurgyis,[16,67] K. Kurita,[60,62] M. Kurosawa,[60,61] Y. Kwon,[76] G. S. Kyle,[53] Y. S. Lai,[12] J. G. Lajoie,[28] D. Larionova,[63] A. Lebedev,[28] B. Lee,[21] D. M. Lee,[39] J. Lee,[17,68] K. B. Lee,[33] K. S. Lee,[33] S. H. Lee,[28,45,67] S. R. Lee,[30] M. J. Leitch,[39] M. A. L. Leite,[64] M. Leitgab,[25] B. Lewis,[67] N. A. Lewis,[45] S. H. Lim,[59,76] L. A. Linden Levy,[11] M. X. Liu,[39] X. Li,[39] D. A. Loomis,[45] B. Love,[73] S. Lökös,[16] C. F. Maguire,[73] T. Majoros,[15] Y. I. Makdisi,[6] M. Makek,[74,77] A. Manion,[67] V. I. Manko,[34] E. Mannel,[7,12] S. Masumoto,[10,32] M. McCumber,[11,39] P. L. McGaughey,[39] D. McGlinchey,[11,19,39] C. McKinney,[25] M. Mendoza,[8] B. Meredith,[25] Y. Miake,[72] T. Mibe,[32] A. C. Mignerey,[42] A. Milov,[74] D. K. Mishra,[4] J. T. Mitchell,[7] M. Mitrankova,[63] Iu. Mitrankov,[63] Y. Miyachi,[60,71] S. Miyasaka,[60,71] A. K. Mohanty,[4] S. Mohapatra,[66] M. M. Mondal,[67] H. J. Moon,[48] T. Moon,[33] D. P. Morrison,[7] S. Motschwiller,[47] T. V. Moukhanova,[34] A. Muhammad,[46] B. Mulilo,[33,60,78] T. Murakami,[35,60] J. Murata,[60,62] A. Mwai,[66] T. Nagae,[35] S. Nagamiya,[32,60] J. L. Nagle,[11] M. I. Nagy,[16,75] I. Nakagawa,[60,61] Y. Nakamiya,[22] K. R. Nakamura,[35,60] T. Nakamura,[60] K. Nakano,[60,71] C. Nattrass,[69] A. Nederlof,[47] S. Nelson,[18] M. Nihashi,[22,60] R. Nouicer,[7,61] T. Novák,[44,75] N. Novitzky,[31,67,72] G. Nukazuka,[60,61] A. S. Nyanin,[34] E. O'Brien,[7] C. A. Ogilvie,[28] J. Oh,[59] K. Okada,[61] M. Orosz,[15] J. D. Osborn,[6,45,56] A. Oskarsson,[41] M. Ouchida,[22,60] K. Ozawa,[10,32,72] R. Pak,[7] V. Pantuev,[26] V. Papavassiliou,[53] B. H. Park,[21] I. H. Park,[17,68] J. S. Park,[65] S. Park,[46,65,67] S. K. Park,[33] L. Patel,[20] M. Patel,[28] S. F. Pate,[53] H. Pei,[28] J.-C. Peng,[25] W. Peng,[73] H. Pereira,[14] D. V. Perepelitsa,[11,12] D. Yu. Peressounko,[34] C. E. PerezLara,[67] R. Petti,[7,67] C. Pinkenburg,[7] R. P. Pisani,[7] M. Potekhin,[7] M. Proissl,[67] A. Pun,[55] M. L. Purschke,[7] H. Qu,[1] P. V. Radzevich,[63] J. Rak,[31] N. Ramasubramanian,[67] I. Ravinovich,[74] K. F. Read,[56,69] D. Reynolds,[66] V. Riabov,[51,58] Y. Riabov,[58,63] E. Richardson,[42] D. Richford,[5] D. Roach,[73] G. Roche,[40,*] S. D. Rolnick,[8] M. Rosati,[28] J. Runchey,[28] B. Sahlmueller,[67] N. Saito,[32] T. Sakaguchi,[7] H. Sako,[29] V. Samsonov,[51,58] M. Sano,[72] M. Sarsour,[20] S. Sato,[29] S. Sawada,[32] K. Sedgwick,[8] R. Seidl,[60,61] A. Sen,[20,28] R. Seto,[8] D. Sharma,[67,74] I. Shein,[24] Z. Shi,[39] M. Shibata,[50] T.-A. Shibata,[60,71] K. Shigaki,[22] M. Shimomura,[28,50,72] K. Shoji,[35,60] P. Shukla,[4] A. Sickles,[7,25] C. L. Silva,[28,39] D. Silvermyr,[41,56] K. S. Sim,[33] B. K. Singh,[3] C. P. Singh,[3] V. Singh,[3] M. Slunečka,[9] K. L. Smith,[19] R. A. Soltz,[38] W. E. Sondheim,[39] S. P. Sorensen,[69] I. V. Sourikova,[7] P. W. Stankus,[56] E. Stenlund,[41] M. Stepanov,[43,*] A. Ster,[75] S. P. Stoll,[7] T. Sugitate,[22] A. Sukhanov,[7] J. Sun,[67] Z. Sun,[15] J. Sziklai,[75] E. M. Takagui,[64] R. Takahama,[50] A. Takahara,[10] A. Taketani,[60,61] Y. Tanaka,[49] S. Taneja,[67] K. Tanida,[29,61,65] M. J. Tannenbaum,[7] S. Tarafdar,[3,73] A. Taranenko,[51,66] E. Tennant,[53] H. Themann,[67] T. Todoroki,[60,61,72] L. Tomášek,[27] M. Tomášek,[13,27] H. Torii,[22] R. S. Towell,[1] I. Tserruya,[74] Y. Tsuchimoto,[10] T. Tsuji,[10] Y. Ueda,[22] B. Ujvari,[15] C. Vale,[7] H. W. van Hecke,[39] M. Vargyas,[16,75] E. Vazquez-Zambrano,[12] A. Veicht,[12] R. Vértesi,[75] J. Velkovska,[73] M. Virius,[13]

*Deceased

†PHENIX spokesperson: akiba@rcf.rhic.bnl.gov

A. Vossen,[25] V. Vrba,[13,27] E. Vznuzdaev,[58] X. R. Wang,[53,61] Z. Wang,[5] D. Watanabe,[22] K. Watanabe,[72] Y. Watanabe,[60,61] Y. S. Watanabe,[10] F. Wei,[28,53] R. Wei,[66] S. N. White,[7] D. Winter,[12] S. Wolin,[25] C. P. Wong,[20,39] C. L. Woody,[7] M. Wysocki,[11,56] B. Xia,[55] Y. L. Yamaguchi,[10,60,67] R. Yang,[25] A. Yanovich,[24] J. Ying,[20] S. Yokkaichi,[60,61] I. Younus,[37,52] Z. You,[39] I. E. Yushmanov,[34] W. A. Zajc,[12] A. Zelenski,[6] and L. Zou[8]

(PHENIX Collaboration)

[1]*Abilene Christian University, Abilene, Texas 79699, USA*
[2]*Department of Physics, Augustana University, Sioux Falls, South Dakota 57197, USA*
[3]*Department of Physics, Banaras Hindu University, Varanasi 221005, India*
[4]*Bhabha Atomic Research Centre, Bombay 400 085, India*
[5]*Baruch College, City University of New York, New York, New York 10010, USA*
[6]*Collider-Accelerator Department, Brookhaven National Laboratory, Upton, New York 11973-5000, USA*
[7]*Physics Department, Brookhaven National Laboratory, Upton, New York 11973-5000, USA*
[8]*University of California-Riverside, Riverside, California 92521, USA*
[9]*Charles University, Ovocný trh 5, Praha 1, 116 36 Prague, Czech Republic*
[10]*Center for Nuclear Study, Graduate School of Science, University of Tokyo, 7-3-1 Hongo, Bunkyo, Tokyo 113-0033, Japan*
[11]*University of Colorado, Boulder, Colorado 80309, USA*
[12]*Columbia University, New York, New York 10027 and Nevis Laboratories, Irvington, New York 10533, USA*
[13]*Czech Technical University, Zikova 4, 166 36 Prague 6, Czech Republic*
[14]*Dapnia, CEA Saclay, F-91191, Gif-sur-Yvette, France*
[15]*Debrecen University, H-4010 Debrecen, Egyetem tér 1, Hungary*
[16]*ELTE, Eötvös Loránd University, H-1117 Budapest, Pázmány P. s. 1/A, Hungary*
[17]*Ewha Womans University, Seoul 120-750, Korea*
[18]*Florida A&M University, Tallahassee, Florida 32307, USA*
[19]*Florida State University, Tallahassee, Florida 32306, USA*
[20]*Georgia State University, Atlanta, Georgia 30303, USA*
[21]*Hanyang University, Seoul 133-792, Korea*
[22]*Hiroshima University, Kagamiyama, Higashi-Hiroshima 739-8526, Japan*
[23]*Department of Physics and Astronomy, Howard University, Washington DC 20059, USA*
[24]*IHEP Protvino, State Research Center of Russian Federation, Institute for High Energy Physics, Protvino 142281, Russia*
[25]*University of Illinois at Urbana-Champaign, Urbana, Illinois 61801, USA*
[26]*Institute for Nuclear Research of the Russian Academy of Sciences, prospekt 60-letiya Oktyabrya 7a, Moscow 117312, Russia*
[27]*Institute of Physics, Academy of Sciences of the Czech Republic, Na Slovance 2, 182 21 Prague 8, Czech Republic*
[28]*Iowa State University, Ames, Iowa 50011, USA*
[29]*Advanced Science Research Center, Japan Atomic Energy Agency, 2-4 Shirakata Shirane, Tokai-mura, Naka-gun, Ibaraki-ken 319-1195, Japan*
[30]*Jeonbuk National University, Jeonju 54896, Korea*
[31]*Helsinki Institute of Physics and University of Jyväskylä, P.O.Box 35, FI-40014 Jyväskylä, Finland*
[32]*KEK, High Energy Accelerator Research Organization, Tsukuba, Ibaraki 305-0801, Japan*
[33]*Korea University, Seoul 02841, Korea*
[34]*National Research Center "Kurchatov Institute", Moscow 123098, Russia*
[35]*Kyoto University, Kyoto 606-8502, Japan*
[36]*Laboratoire Leprince-Ringuet, Ecole Polytechnique, CNRS-IN2P3, Route de Saclay, F-91128 Palaiseau, France*
[37]*Physics Department, Lahore University of Management Sciences, Lahore 54792, Pakistan*
[38]*Lawrence Livermore National Laboratory, Livermore, California 94550, USA*
[39]*Los Alamos National Laboratory, Los Alamos, New Mexico 87545, USA*
[40]*LPC, Université Blaise Pascal, CNRS-IN2P3, Clermont-Fd, 63177 Aubiere Cedex, France*
[41]*Department of Physics, Lund University, Box 118, SE-221 00 Lund, Sweden*
[42]*University of Maryland, College Park, Maryland 20742, USA*
[43]*Department of Physics, University of Massachusetts, Amherst, Massachusetts 01003-9337, USA*
[44]*MATE, Laboratory of Femtoscopy, Károly Róbert Campus, H-3200 Gyöngyös, Mátraiút 36, Hungary*
[45]*Department of Physics, University of Michigan, Ann Arbor, Michigan 48109-1040, USA*
[46]*Mississippi State University, Mississippi State, Mississippi 39762, USA*
[47]*Muhlenberg College, Allentown, Pennsylvania 18104-5586, USA*
[48]*Myongji University, Yongin, Kyonggido 449-728, Korea*
[49]*Nagasaki Institute of Applied Science, Nagasaki-shi, Nagasaki 851-0193, Japan*
[50]*Nara Women's University, Kita-uoya Nishi-machi, Nara 630-8506, Japan*
[51]*National Research Nuclear University, MEPhI, Moscow Engineering Physics Institute, Moscow 115409, Russia*
[52]*University of New Mexico, Albuquerque, New Mexico 87131, USA*

[53]*New Mexico State University, Las Cruces, New Mexico 88003, USA*
[54]*Physics and Astronomy Department, University of North Carolina at Greensboro, Greensboro, North Carolina 27412, USA*
[55]*Department of Physics and Astronomy, Ohio University, Athens, Ohio 45701, USA*
[56]*Oak Ridge National Laboratory, Oak Ridge, Tennessee 37831, USA*
[57]*IPN-Orsay, Univ. Paris-Sud, CNRS/IN2P3, Université Paris-Saclay, BP1, F-91406 Orsay, France*
[58]*PNPI, Petersburg Nuclear Physics Institute, Gatchina, Leningrad region 188300, Russia*
[59]*Pusan National University, Pusan 46241, Korea*
[60]*RIKEN Nishina Center for Accelerator-Based Science, Wako, Saitama 351-0198, Japan*
[61]*RIKEN BNL Research Center, Brookhaven National Laboratory, Upton, New York 11973-5000, USA*
[62]*Physics Department, Rikkyo University, 3-34-1 Nishi-Ikebukuro, Toshima, Tokyo 171-8501, Japan*
[63]*Saint Petersburg State Polytechnic University, St. Petersburg 195251, Russia*
[64]*Universidade de São Paulo, Instituto de Física, Caixa Postal 66318, São Paulo CEP05315-970, Brazil*
[65]*Department of Physics and Astronomy, Seoul National University, Seoul 151-742, Korea*
[66]*Chemistry Department, Stony Brook University, SUNY, Stony Brook, New York 11794-3400, USA*
[67]*Department of Physics and Astronomy, Stony Brook University, SUNY, Stony Brook, New York 11794-3800, USA*
[68]*Sungkyunkwan University, Suwon 440-746, Korea*
[69]*University of Tennessee, Knoxville, Tennessee 37996, USA*
[70]*Texas Southern University, Houston, Texas 77004, USA*
[71]*Department of Physics, Tokyo Institute of Technology, Oh-okayama, Meguro, Tokyo 152-8551, Japan*
[72]*Tomonaga Center for the History of the Universe, University of Tsukuba, Tsukuba, Ibaraki 305, Japan*
[73]*Vanderbilt University, Nashville, Tennessee 37235, USA*
[74]*Weizmann Institute, Rehovot 76100, Israel*
[75]*Institute for Particle and Nuclear Physics, Wigner Research Centre for Physics, Hungarian Academy of Sciences (Wigner RCP, RMKI) H-1525 Budapest 114, PO Box 49, Budapest, Hungary*
[76]*Yonsei University, IPAP, Seoul 120-749, Korea*
[77]*Department of Physics, Faculty of Science, University of Zagreb, Bijenička c. 32 HR-10002 Zagreb, Croatia*
[78]*Department of Physics, School of Natural Sciences, University of Zambia, Great East Road Campus, Box 32379, Lusaka, Zambia*

(Received 24 March 2022; accepted 21 October 2022; published 24 February 2023)

The measurement of direct photons from Au + Au collisions at $\sqrt{s_{NN}} = 39$ and 62.4 GeV in the transverse-momentum range $0.4 < p_T < 3$ Gev/c is presented by the PHENIX collaboration at the BNLRelativistic Heavy Ion Collider. A significant direct-photon yield is observed in both collision systems. A universal scaling is observed when the direct-photon p_T spectra for different center-of-mass energies and for different centrality selections at $\sqrt{s_{NN}} = 62.4$ GeV is scaled with $(dN_{\rm ch}/d\eta)^{\alpha}$ for $\alpha = 1.21 \pm 0.04$. This scaling also holds true for direct-photon spectra from Au + Au collisions at $\sqrt{s_{NN}} = 200$ GeV measured earlier by PHENIX, as well as the spectra from Pb + Pb at $\sqrt{s_{NN}} = 2760$ GeV published by ALICE. The scaling power α seems to be independent of p_T, center of mass energy, and collision centrality. The spectra from different collision energies have a similar shape up to p_T of 2 Gev/c. The spectra have a local inverse slope $T_{\rm eff}$ increasing with p_T of 0.174 ± 0.018 Gev/c in the range $0.4 < p_T < 1.3$ Gev/c and increasing to 0.289 ± 0.024 Gev/c for $0.9 < p_T < 2.1$ Gev/c. The observed similarity of low-p_T direct-photon production from $\sqrt{s_{NN}} = 39$ to 2760 GeV suggests a common source of direct photons for the different collision energies and event centrality selections, and suggests a comparable space-time evolution of direct-photon emission.

DOI: 10.1103/PhysRevC.107.024914

I. INTRODUCTION

The measurement of direct-photon emission plays an important role in the study of collisions of heavy ions [1–4]. Due to their very small interaction cross section with the strongly interacting matter, photons are likely to escape the collision region with almost no final-state interactions. Thus, they carry information about the properties and dynamics of the environment in which they are produced, such as the energy density, temperature, and collective motion, integrated over space and time.

Direct photons with transverse momenta (p_T) of up to a few GeV/c are expected to be dominantly of thermal origin, radiated from a thermalized hot "fireball" of quark-gluon plasma (QGP), throughout its expansion and transition to a gas of hadrons, until the hadrons cease to interact. In addition to the fireball, hard-scattering processes in the initial phase of the collision also emit photons. These prompt photons typically have larger p_T and dominate the direct-photon production at p_T above several GeV/c. Experimentally, direct photons are measured together with a much larger number of photons resulting from decays of unstable hadrons, such as π^0 and η decays. The contribution of these decay photons to the total number of photons needs to be removed with an accuracy of a few percent, which is the main experimental challenge.

The production of thermal photons has been extensively studied through a variety of models with different production processes and mechanisms, different photon rates, as well as a range of assumptions about the initial state of the matter and its space-time evolution. Some of the well-known examples include models developed with an "elliptic-fireball" expansion approach [5,6], hydrodynamic simulations of the "fireball" evolution [7–10], the parton-hadron-string dynamics transport approach [11–13], the thermalizing glasma [14–17] and the thermalizing glasma plus bottom-up thermalization scenarios for calculations of the pre-equilibrium and equilibrium phases [18,19], reduced radiation from the QGP until the transition temperature is reached [20,21], as well as calculations in the late hadron-gas phase using the spectral-function approach [21–26]. The strong magnetic fields emerging in heavy ion collisions have been considered as an additional, significant source of photons [27–30].

The PHENIX experiment at the BNL Relativistic Heavy Ion Collider (RHIC) was the first to detect a large yield of direct photons in heavy ion collisions at $\sqrt{s_{NN}} = 200$ GeV [31]. Earlier evidence was presented by the WA98 collaboration [32,33] for $\sqrt{s_{NN}} = 17.3$ GeV, with mostly upper limits below 1.5 GeV/c in p_T, except for two points obtained from interferometry in the 0.1–0.3 GeV/c p_T range, which is below our p_T threshold. Multiple subsequent publications from PHENIX established that at RHIC energies the direct-photon yield below transverse momenta of 2 GeV/c exceeded what was expected from hard processes by a factor of ≈ 10 [34], showed a stronger-than-linear increase with the collision volume [35], and a large anisotropy with respect to the reaction plane [36,37]. The STAR collaboration also reported an enhanced yield of direct photons at low p_T in Au+Au collisions at $\sqrt{s_{NN}} = 200$ GeV [38]; for minimum bias (MB) events the yield measured by STAR is a factor of ≈3 lower for p_T below 2 GeV/c, while it is consistent at higher p_T.[1] Observations consistent with the PHENIX Au+Au measurements at $\sqrt{s_{NN}} = 200$ GeV were made by the ALICE Collaboration at the CERN Large Hadron Collider (LHC) [39] in Pb+Pb collisions at $\sqrt{s_{NN}} = 2.76$ TeV and, more recently, by PHENIX at the lower energies of 39 and 62.4 GeV [40]. The low transverse-momentum yield, for p_T below 2 GeV/c, shows a power-law dependence on $dN_{\rm ch}/d\eta|_{\eta\approx 0}$ with a power $\alpha \approx 1.25$ [40]. The power α is independent of centrality or collision energy.[2] These experimental findings are qualitatively consistent with thermal radiation being emitted from a rapidly expanding and cooling fireball. However, it is challenging for theoretical models to describe all data quantitatively.

To further constrain the sources of low-momentum direct photons, PHENIX continues its program on such measurements in large- and small-system collisions. This paper extends a previous publication on Au + Au collisions at $\sqrt{s_{NN}} = 39$ and 62.4 GeV [40] and provides more detail about the measurement and the universal features exhibited by direct photons emitted from heavy ion collisions from RHIC to LHC energies, including inverse slopes and the scaling with $dN_{\rm ch}/d\eta$, both as a function of p_T.

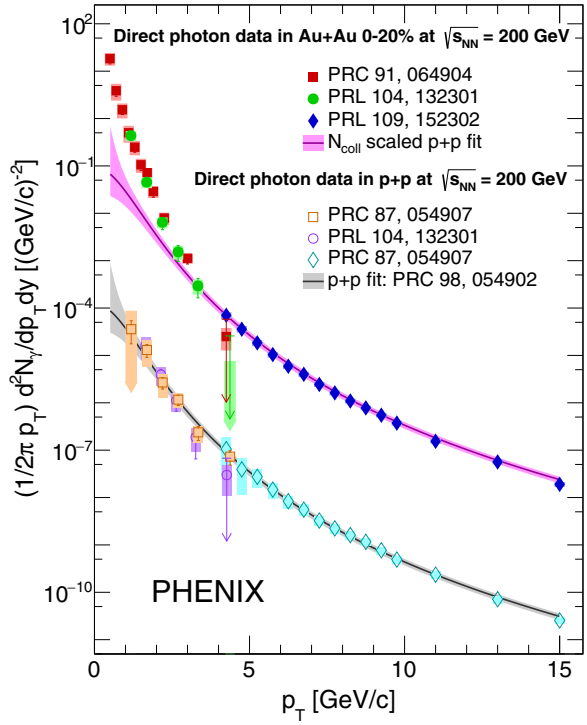

FIG. 1. The upper data points are the invariant yield of direct photons in Au+Au collisions in 0%–20% centrality bin at 200 GeV: the full square data are from an analysis based on external conversions [35], the full circle data are from an analysis based on internal conversions [34], the full diamond data are from calorimeter measurements [41]. The lower data points are the invariant yield of direct photons in $p + p$ collisions at 200 GeV: the open square and open circle data are from internal conversions [34,42], the open diamond data are from calorimeter measurements [43,44]. The lower curve is a fit to the combined set of $p + p$ data, extrapolated below 1 Gev/c [40,45–47], and the upper curve is the $N_{\rm coll}$ scaled $p + p$ fit with $N_{\rm coll} = 779.0$ [35].

The paper is organized as follows. Section II presents the measurement and the results of low-momentum direct-photon production in Au+Au at $\sqrt{s_{NN}} = 39$ and 62.4 GeV. Section III puts these results into context with other direct-photon measurements. Section IV gives the summary and conclusions.

II. LOW-MOMENTUM DIRECT-PHOTON PRODUCTION AT $\sqrt{s_{NN}} = 39$ AND 62.4 GeV

A. Experimental method for measuring direct photons

Figure 1 presents the direct-photon p_T spectra measured by PHENIX in Au+Au collisions in the 0%–20% centrality bin at $\sqrt{s_{NN}} = 200$ GeV, including data points from an analysis based on external conversions [35], internal conversions [34], and from calorimeter measurements [41]. Also shown are invariant yields of direct photons in $p + p$ collisions at 200 GeV from internal conversions [34,42], calorimeter measurements

[1]The persisting discrepancy between STAR and PHENIX measurements at low p_T is noted, but cannot be resolved by PHENIX alone and thus is not further discussed in this paper.

[2]Throughout the rest of the paper the subscript $\eta \approx 0$ will be dropped and $dN_{\rm ch}/d\eta$ will always imply density at midrapidity.

[43,44], a fit to the combined set of $p+p$ data, extrapolated below 1 Gev/c [40,45–47], and an $N_{\rm coll}$-scaled $p+p$ fit with $N_{\rm coll} = 779.0$ [35].

The three techniques used for measuring direct photons deploy different detector systems within the PHENIX central arms[3] (see Ref. [48]) and various strategies to extract the direct photons from the decay-photon background include measuring:

(i) photons that directly deposit energy into electromagnetic calorimeters. This is the method of choice to measure high momentum photons. At p_T below a few GeV/c, the method suffers from significant background contamination from hadrons depositing energy in the calorimeter and the limited energy resolution [41].

(ii) virtual photons that internally convert into e^+e^- pairs and extrapolating their measured yield to zero mass. This technique was used for the original discovery of low-momentum direct photons at RHIC [34]. The pairs are measured in the mass region above the π^0 mass, which eliminates more than 90% of the hadron-decay-photon background. The extrapolation to zero mass requires the pair mass to be much smaller than the pair momentum, and thus limits the measurement to $p_T > 1$ GeV/c.

(iii) photons that convert to e^+e^- pairs in the detector material ("external conversion method"). This method gives access to a nearly background-free sample of photons down to p_T below 1 GeV/c [35].

The external-conversion method is used for the analysis presented here, which is the identical method used to analyze direct-photon production from 2010 Au+Au collisions at $\sqrt{s_{NN}} = 200$ GeV [35,37]. Additional details can be found in Ref. [49]. The analysis proceeds in multiple steps. First established is $N_\gamma^{\rm incl}$, which is a sample of conversion photons measured in the PHENIX-detector acceptance. This is done in bins of conversion photon p_T. For a given p_T selection, the $N_\gamma^{\rm incl}$ sample relates to the true number of photons $\gamma^{\rm incl}$ in that p_T range as follows:

$$N_\gamma^{\rm incl} = \varepsilon_{ee} a_{ee}\, p_{\rm conv}\, \gamma^{\rm incl}, \tag{1}$$

where a_{ee} is the e^+e^- pair acceptance, ε_{ee} is the pair reconstruction efficiency, and $p_{\rm conv}$ is the conversion probability. In the next step a subsample $N_\gamma^{\pi^0,{\rm tag}}$ of $N_\gamma^{\rm incl}$ is tagged as π^0 decay photons; details of how the $N_\gamma^{\pi^0,{\rm tag}}$ subsample is determined are described in Sec. II C below. Because $N_\gamma^{\pi^0,{\rm tag}}$ is a subset of $N_\gamma^{\rm incl}$, it is related to the true number of π^0 decay photons γ^{π^0} among $\gamma^{\rm incl}$ by

$$N_\gamma^{\pi^0,{\rm tag}} = \varepsilon_{ee} a_{ee}\, p_{\rm conv}\, \langle \varepsilon_\gamma f \rangle \gamma^{\pi^0} \tag{2}$$

with $\langle \varepsilon_\gamma f \rangle$ being the average conditional probability of detecting the second photon in the PHENIX acceptance, given that one π^0 decay photon converted and was reconstructed in the desired conversion photon p_T range. Here the average is taken over all possible π^0 p_T. Taking the ratio of Eqs. (1) and (2) gives

$$\frac{\gamma^{\rm incl}}{\gamma^{\pi^0}} = (\langle \varepsilon_\gamma f \rangle)_{\rm Sim} \left(\frac{N_\gamma^{\rm incl}}{N_\gamma^{\pi^0,{\rm tag}}} \right)_{\rm Data}. \tag{3}$$

This ratio is constructed such that $\varepsilon_{ee} a_{ee}\, p_{\rm conv}$ explicitly cancels, eliminating the need to determine these quantities and the related systematic uncertainties. The only correction necessary is the conditional probability $\langle \varepsilon_\gamma f \rangle$, which is determined from a full Monte Carlo simulation of the PHENIX detector indicated by the subscript $_{\rm Sim}$. The second factor is a ratio of directly measured quantities, indicated by $_{\rm Data}$. Finally, Eq. (3) can be divided by the fraction of hadron decay photons ($\gamma^{\rm hadr}$) per π^0 decay photon, which defines R_γ as a double ratio

$$R_\gamma = \frac{\gamma^{\rm incl}}{\gamma^{\rm hadr}} = \frac{(\langle \varepsilon_\gamma f \rangle)_{\rm Sim} \left(N_\gamma^{\rm incl} / N_\gamma^{\pi^0,{\rm tag}} \right)_{\rm Data}}{(\gamma^{\rm hadr}/\gamma^{\pi^0})_{\rm Gen}}. \tag{4}$$

where the ratio $\gamma^{\rm hadr}/\gamma^{\pi^0}$ was determined with a particle-decay generator, indicated by the subscript $_{\rm Gen}$.

If direct photons are emitted from the collision system in a particular p_T range, R_γ will be larger than unity. The denominator in Eq. (4) can be obtained from the PHENIX hadron-decay generator EXODUS [50], based on the measured π^0 spectra. In the following sections, the determination of $N_\gamma^{\rm incl}$, $N_\gamma^{\pi^0,{\rm tag}}$, $\langle \varepsilon_\gamma f \rangle$, and $\gamma^{\rm hadr}/\gamma^{\pi^0}$ will be discussed separately.

B. Determining the inclusive photon sample $N_\gamma^{\rm incl}$

The 2010 data samples of 7.79×10^7 (at 39 GeV) and 2.12×10^8 (at 62.4 GeV) MB Au + Au collisions were recorded with the two PHENIX central-arm spectrometers, each of which has an acceptance of $\pi/2$ in azimuthal angle and $|\eta| < 0.35$ in pseudorapidity. For both collision energies, the MB data sets cover a range of 0%–86% of the interaction cross section. The data sample for 62.4 GeV is large enough so that two centrality classes (0%–20% central collisions, 20%–40% midcentral collisions) could be analyzed separately. The event centrality is categorized by the charge measured in the PHENIX beam-beam counters [51], which are located at a distance of 144 cm from the nominal interaction point in both beam directions, covering the pseudorapidity range of $3.1 < |\eta| < 3.9$ and 2π in azimuth.

The PHENIX central-arm drift chambers and pad chambers [52], located from 200 to 250 cm radially to the beam axis, are used to determine the trajectories and momenta of charged particles. The momenta are measured assuming the track originated at the event vertex (vtx) and traversed the full magnetic field. The tracks are identified as electrons or positrons by a combination of a minimum signal in the ring-imaging Čerenkov (RICH) detector [53] and a match of the track momentum with the energy measured in the electromagnetic calorimeter (EMCal) [54]. The RICH cut requires that a minimum of three RICH phototubes be matched to the

[3]The PHENIX central arm acceptance is 0.7 units around midrapidity. Thus there is little difference between momentum and transverse momentum, so the terms will be used interchangeably in the following discussion.

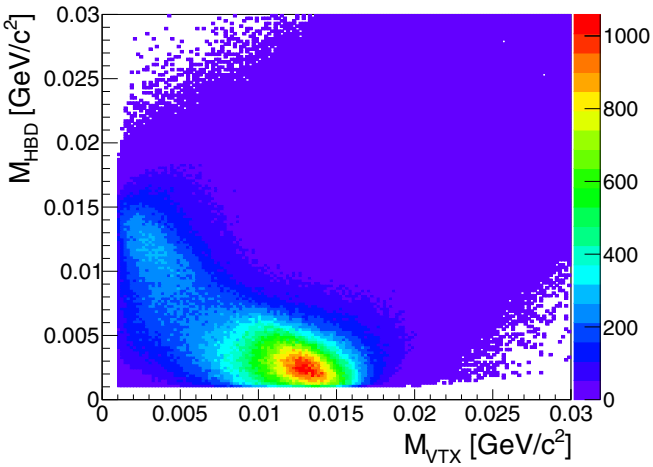

FIG. 2. Mass correlation of e^+e^- pairs measured in Au+Au collisions at $\sqrt{s_{NN}} = 62.4$ GeV. Conversion photon e^+e^- pairs are identified by the correlation between the mass calculated assuming the track originated at the interaction point ($M_{\rm vtx}$) or at the HBD back plane ($M_{\rm HBD}$).

charged track within a radius interval of 3.4 cm $< r <$ 8.4 cm at the expected ring location. For each electron candidate an associated energy measurement in the EMCal is required, with an energy/momentum ratio, E/p, greater than 0.5. Electrons and positrons are combined to e^+e^- pairs and further selection cuts are applied to establish a clean sample of photon conversions. Most photon conversions occur in the readout boards and electronics at the back plane of the hadron blind detector (HBD) [55], located at a radius of ≈ 60 cm from the nominal beam axis. The relative thickness in terms of radiation length is equal to $X/X_0 \approx 2.5\%$; all other material between the beam axis and the drift chamber is significantly thinner. Electrons and positrons from these conversions do not traverse the full magnetic field.[4] Projecting the tracks back to the interaction point results in a small distortion of the reconstructed momenta, both in magnitude and in direction, which in turn results in an artificial opening angle of the e^+e^- pair. This gives the pair an apparent mass ($M_{\rm vtx}$), which depends monotonically on the radial location of the conversion point and is approximately 0.0125 GeV/c^2 for conversions in the HBD back plane.

To select photon conversions in the HBD back plane, the track momenta are re-evaluated assuming the tracks originated at the HBD back plane. For e^+e^- pair from conversions in the HBD back plane, a mass ($M_{\rm HBD}$) of below 0.005 GeV/c^2 is calculated with a distribution expected for an e^+e^- pair of zero mass measured with the PHENIX-detector resolution. Figure 2 shows the correlation between the two different masses calculated for each pair. Photon conversions in the HBD back plane are clearly separated from e^+e^- pairs from π^0 Dalitz decays, $\pi^0 \to \gamma e^+e^-$, which populate a region $M_{\rm vtx} < 0.005$ GeV/c^2 and $M_{\rm HBD}$ around 0.012 GeV/c^2. The region between the e^+e^- pairs from Dalitz decays and conversion in the HBD back plane is populated by conversions at radii smaller than 60 cm. To select a clean sample of photon conversions in the HBD back plane, $N_\gamma^{\rm incl}$, a two-dimensional cut is applied: $M_{\rm HBD} < 0.0045$ GeV/c^2 and $0.01 < M_{\rm vtx} < 0.015$ GeV/c^2. The purity of this photon sample was determined with a full Monte Carlo simulation and is better than 99%. The sample sizes are 9.42×10^4 and 3.28×10^5, for 39 and 62.4 GeV, respectively.

C. Tagging photons from $\pi^0 \to \gamma\gamma$ decays

Once the conversion-photon sample $N_\gamma^{\rm incl}$ is established, all e^+e^- pairs in a given p_T bin are combined with showers reconstructed in the EMCal in the same event and then the invariant mass is calculated. A minimum-energy cut of 0.4 GeV is applied to remove charged particles that leave a minimum-ionizing signal in the EMCal and further reduce the hadron contamination by applying a shower-shape cut. Figure 3(a) shows one example of the resulting mass distributions for a p_T bin around 1 GeV/c from the 62.4-GeV MB data set. The π^0 peak is clearly visible above a combinatorial background, which results from combining e^+e^- pairs with all showers in the event, most of which are not correlated with the e^+e^- pair.

A mixed-event technique is used to determine and subtract the mass distribution of these random combinations. In event mixing, all e^+e^- pairs in a given event are combined with the EMCal showers from several other events. These other events are chosen to be in the same 10% centrality selection and within 1 cm of the interaction point of the event with the e^+e^- pair. The ratio of the measured (foreground) mass distribution and mixed event (background) mass distribution is fitted with a second-order polynomial, excluding the mass range $0.08 < m_{ee\gamma} < 0.19$ GeV/c^2, around the π^0 peak. Figure 3(b) shows the ratio and the fit, which is used to normalize the mixed event background distribution over the full mass range; the result is included in Fig. 3(b).

Figure 3(c) depicts the counts remaining after the mixed event background distribution is subtracted from the foreground distribution. The raw yield of tagged π^0 is calculated as the sum of all counts in mass window $0.11 < m_{ee\gamma} < 0.165$ GeV/c^2. The counts in two side bands around the π^0 peak are evaluated to account for any possible remaining mismatch of the shape of the combinatorial background from mixed events compared to the true shape. These side bands are $0.035 < m_{ee\gamma} < 0.110$ GeV/c^2 and $0.165 < m_{ee\gamma} < 0.240$ GeV/c^2. The average counts per mass bin in the side bands is subtracted from the raw tagged π^0 counts, the resulting counts are the number of tagged π^0, $N_\gamma^{\pi^0,{\rm tag}}$ in the given p_T bin.

Figure 4 shows both $N_\gamma^{\rm incl}$ and $N_\gamma^{\pi^0,{\rm tag}}$ for 39 and 62.4 GeV MB Au+Au data. Figure 5 gives the ratios, $N_\gamma^{\rm incl}/N_\gamma^{\pi^0,{\rm tag}}$.

The systematic uncertainties of the peak-extraction procedure were evaluated by choosing different-order polynomial function for the normalization and the various mass windows

[4] A special field configuration was used in 2010 for the operation of the HBD. In this configuration there is a nearly field free region around the beam axis out to 60 cm. Thus the field integral missed by tracks from photon conversions in the HBD back plane is rather small.

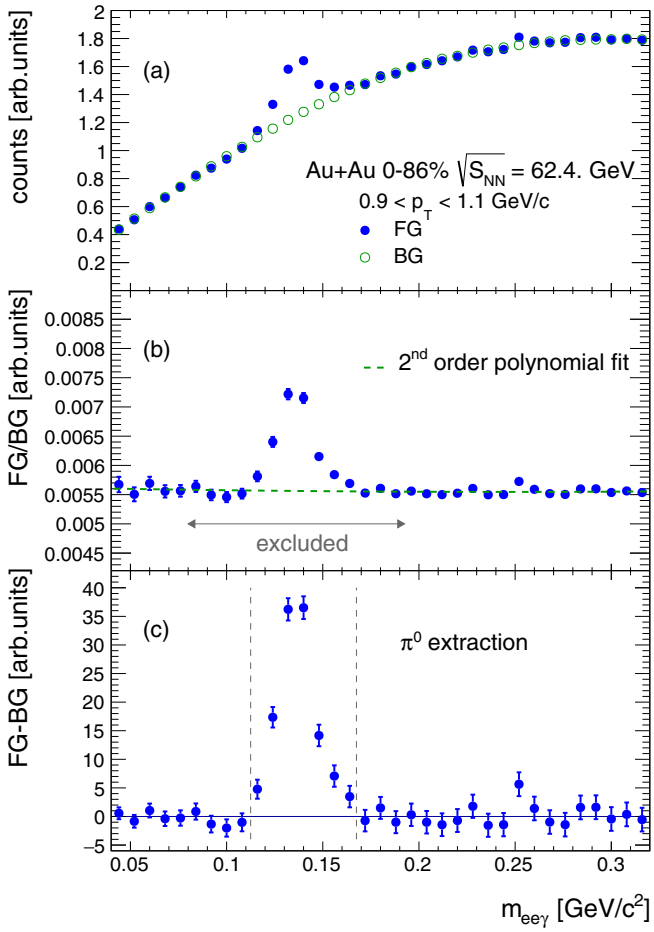

FIG. 3. Illustration of the π^0 peak extraction method for one p_T bin from 0.9 to 1.1 GeV/c in MB Au+Au collisions at $\sqrt{s_{NN}}$ = 64 GeV. (a) shows the e^+e^- γ foreground (FG) and the normalized mixed-event background (BG). (b) gives the ratio of foreground to background used to normalize the mixed event background. (c) presents the counts after subtracting the normalized mixed-event background.

were varied in the procedure. It is found that $N_\gamma^{\pi^0,\mathrm{tag}}$ changes by less than 8% and 5% for 39 and 62.4 GeV data, respectively. These systematic uncertainties are mostly uncorrelated between p_T bins and thus are added in quadrature to the statistical uncertainties on $N_\gamma^{\pi^0,\mathrm{tag}}$.

D. The conditional π^0 tagging probability

The conditional probability $\langle \varepsilon_\gamma f \rangle$, to tag an e^+e^- pair that resulted from a conversion of a π^0 decay photon with the second decay photon, depends on the parent π^0 p_T spectrum, the π^0 decay kinematics, the detector acceptance, and, the photon reconstruction efficiency. A Monte Carlo method is used to calculate $\langle \varepsilon_\gamma f \rangle$. The method was developed for the direct-photon measurement from Au+Au collisions at $\sqrt{s_{NN}}$ = 200 GeV, also recorded during 2010, as described in Ref. [35]. The calculation is done separately for MB and centrality selected Au+Au collisions at 39 and 62.4 GeV.

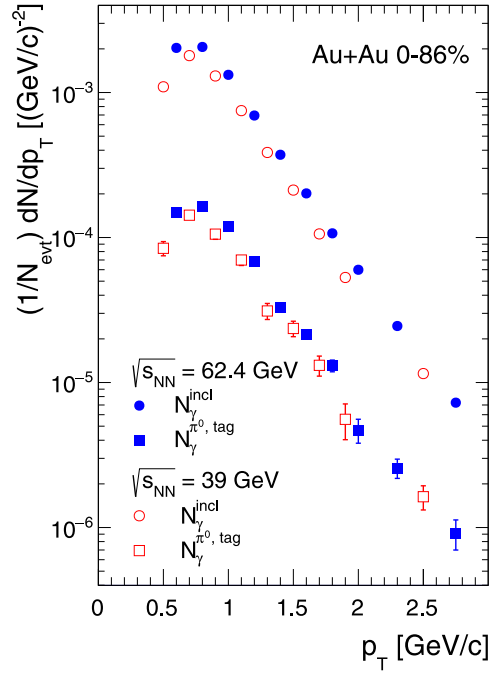

FIG. 4. Raw counts of N_γ^{incl} and its subsample $N_\gamma^{\pi^0,\mathrm{tag}}$, which was tagged as photons from π^0 decays. Data for MB Au+Au collisions from 39 and 62.4 GeV are given.

Each calculation is based on an input π^0 spectrum that was measured for the same data sample [56].

Figure 6 shows the results for MB collisions. The conditional probability $\langle \varepsilon_\gamma f \rangle$ is small; it increases from approximately 10% to 20% over the p_T range from 0.8 to 2.5 GeV/c. The visible difference between $\langle \varepsilon_\gamma f \rangle$ for 39 and 62.4 GeV is due to the $\sqrt{s}$ dependence of the π^0 p_T spectra, which are much softer for the lower energies. Because $\langle \varepsilon_\gamma f \rangle$ is evaluated for a fixed p_T range of the e^+e^- pair, it is averaged over all possible π^0 p_T. Thus the value of $\langle \varepsilon_\gamma f \rangle$ at a fixed e^+e^- pair p_T is sensitive to the parent π^0 p_T spectrum.

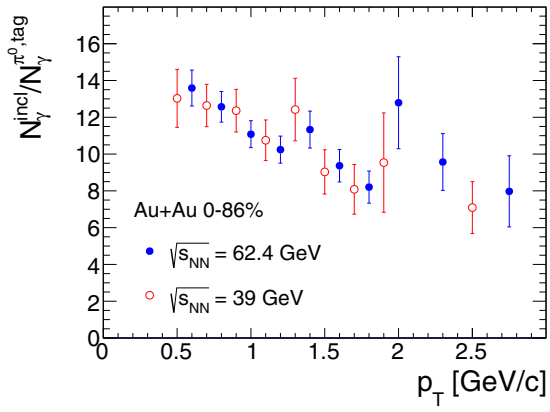

FIG. 5. The ratio of the measured inclusive photon yield N_γ^{incl} to the yield $N_\gamma^{\pi^0,\mathrm{tag}}$ of those photons tagged as π^0 decay photons for MB data samples at $\sqrt{s_{NN}}$ = 39 and 62.4 GeV. The x axis is the p_T of the e^+e^- pair.

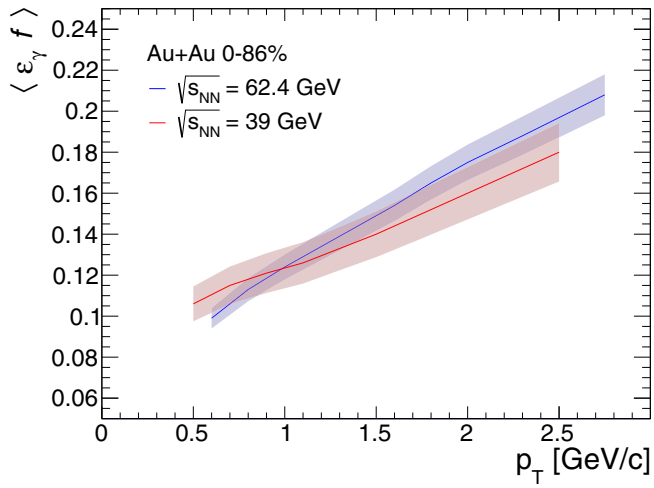

FIG. 6. Simulated conditional probability, $\langle \varepsilon_\gamma f \rangle$, to detect the second photon from a π^0 decay in the MB data samples at $\sqrt{s_{NN}} = 39$ and 62.4 GeV. The x axis is the p_T of the e^+e^- pair.

The EMCal acceptance contributes a multiplicative factor of 0.35 to $\langle \varepsilon_\gamma f \rangle$ at an e^+e^- pair $p_T = 0.8$ GeV/c, the factor increases to 0.45 at 2.5 GeV/c. This includes the geometrical dimension and the location of the EMCal sectors, the fiducial cuts around the sector boundaries and any dead areas in the EMCal. The minimum-energy cut of 0.4 GeV is the main contributor to the photon-reconstruction efficiency loss. This cut is equivalent to an asymmetry cut on the π^0 decay photons; the effect being largest at the lowest π^0 momenta that can contribute in a given e^+e^- pair p_T bin. With additional, but small, contributions from the shower-shape cut and the conversion of the second photon, the reconstruction efficiency rises from ≈0.3 to 0.45 over the p_T range of 0.8 to 2.5 GeV/c.

Figure 6 also shows the systematic uncertainties on $\langle \varepsilon_\gamma f \rangle$, which are 8% and 5% for 39 and 62.4 GeV, respectively. The uncertainty of the energy calibration and the accuracy of the π^0 p_T spectra are the two dominant sources of systematic uncertainties. A 2% change in the energy calibration, and with it a change of the actual energy cutoff, modifies $\langle \varepsilon_\gamma f \rangle$ by 3% to 4%. For 62.4 GeV, the measured π^0 p_T spectra agree in shape within ±10% with the charged-pion data from the STAR Collaboration [57]. Possible shape variations within this range translate into an uncertainty of 3% on $\langle \varepsilon_\gamma f \rangle$.

For 39 GeV, STAR has published charged-pion data up to 2 GeV/c [58], these data agree in shape with the PHENIX π^0 data within ±10%. However, due to the limited p_T range, the systematic uncertainties on the shape of the π^0 p_T spectrum were determined from the systematic uncertainties of the PHENIX measurement alone, which is less restrictive and, thus, results in a larger uncertainty.

E. Decay photons form hadron decays

The ratio of all photons from hadron decays to those from π^0 decays, $\gamma^{\rm hadr}/\gamma^{\pi^0}$ in the denominator of Eq. (3), is the final component that is needed to calculate R_γ. In addition to decays of π^0, decays of the η, ω, and η' mesons contribute to $\gamma^{\rm hadr}$, with the η decay being the largest contributor. Any other decays emit a negligible number of photons.

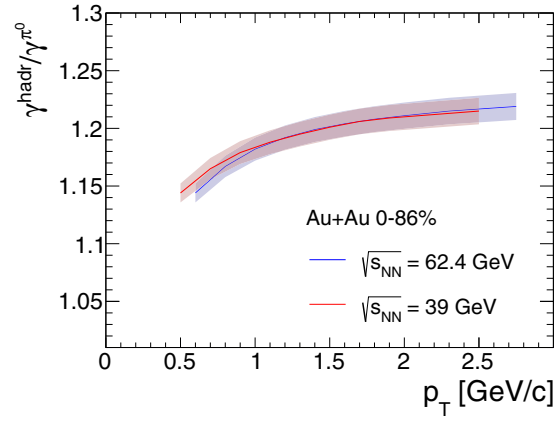

FIG. 7. Simulated ratio of photons from hadron decays to those from π^0 decays in the MB data samples at $\sqrt{s_{NN}} = 39$ and 62.4 GeV. The x axis is the p_T of the e^+e^- pair.

Photons from hadron decays are modeled based on the parent p_T distributions. For each centrality class, the measured π^0 p_T spectrum is used to generate π^0s, which are subsequently decayed to photons using the known branching ratios and decay kinematics. The decay photons from η, ω and η' are modeled similarly, with a parent p_T distribution derived from the measured π^0 p_T distributions, assuming $\boldsymbol{m}_T$ scaling (see Refs. [34,59] for details)[5] The normalization of photons from η, ω, and η' is set to $\eta/\pi^0 = 0.46 \pm 0.06$, $\omega/\pi^0 = 0.9 \pm 0.06$, and $\eta'/\pi^0 = 0.25 \pm 0.075$ all at $p_T = 5$ Gev/c.

Figure 7 shows the $\gamma^{\rm hadr}/\gamma^{\pi^0}$ ratio. The ratio increases with p_T and saturates at high p_T between 1.22 and 1.23. There is no appreciable $\sqrt{s}$ dependence of $\gamma^{\rm hadr}/\gamma^{\pi^0}$. Following Ref. [35], the systematic uncertainties from $\gamma^{\rm hadr}/\gamma^{\pi^0}$ on R_γ are estimated to be 2.4%.

F. Direct-photon spectra

After each factor in Eq. (4) is determined, R_γ can be calculated. Figure 8 shows the results for all centrality classes. Despite the significant statistical and systematic uncertainties, the majority of the data points are above unity at a value around $R_\gamma \approx 1.2$. This indicates the presence of a direct-photon component of ≈20% relative to hadron-decay photons in Au+Au collisions at 39 and 62.4 GeV. There is no

[5]Reference [59] recently noted that using m_T scaling overestimates the η meson yield in $p+p$ collisions for p_T below 2 GeV/c. The same work also shows that in Au+Au collisions at RHIC energies, this depletion is partially compensated by radial flow, which enhances the yield of η in the same p_T region. For this analysis, removing the m_T scaling assumption, while including the effect of radial flow, will reduce the number of photons from hadron decays by ≈2% for $p_T \approx 1$ GeV/c, where the change is the largest. Correspondingly the direct-photon yield would increase by 2%, which is within the systematic errors of 2.4% quoted on the contribution of $\gamma^{\rm hadr}/\gamma^{\pi^0}$ to R_γ and much smaller than the overall statistical (>7%) and systematic (>5%) uncertainties of the R_γ measurement at p_T of 1 GeV/c.

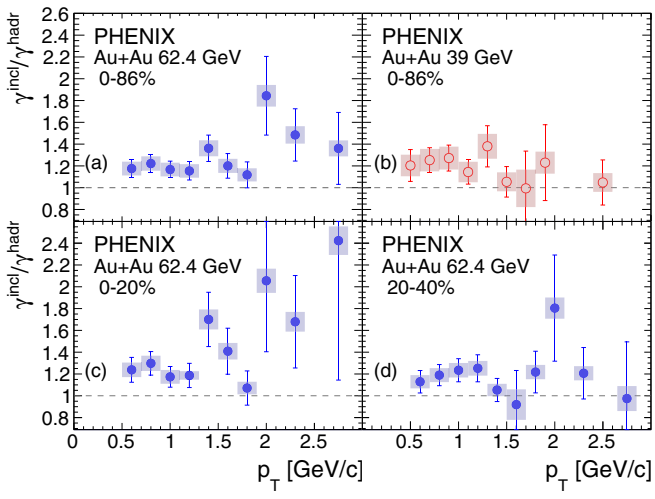

FIG. 8. R_γ ($\gamma^{\rm incl}/\gamma^{\rm hadr}$) for MB (0%–86%) Au+Au collision at $\sqrt{s_{NN}}$ = (a) 62.4 and (b) 39 GeV. Also shown for 62.4 GeV are centrality bins (c) 0%–20% and (d) 20%–40%. Data points are shown with statistical (bar) and systematic (box) uncertainties.

obvious p_T dependence over the observed range; furthermore, the $\sqrt{s}$ and centrality dependence, if any, must be small.

To further analyze the data R_γ is converted to a direct-photon p_T spectrum $\gamma^{\rm dir}$ using the hadron-decay-photon spectra calculated in Sec. II E:

$$\gamma^{\rm dir} = (R_\gamma - 1)\gamma^{\rm hadr}. \tag{5}$$

Figure 9 presents the calculated direct-photon p_T spectra. In addition to the systematic uncertainty on R_γ, the hadron-decay-photon spectra contribute ≈10% to the systematic uncertainties. These uncertainties cancel in $\gamma^{\rm hadr}/\gamma^{\pi^0}$, but need to be considered here. Each centrality and energy selection is compared to the expected prompt-photon contribution from hard-scattering processes based on perturbative-quantum-chromodynamics (pQCD) calculations from [10,60]. Shown are the calculations at the scale $\mu = 0.5\,p_T$, which were extrapolated down to $p_T = 1$ Gev/c. The scale was selected as it typically gives a good description of prompt-photon measurements in $p + p$ collisions (see also Fig. 10). To represent hard scattering in Au+Au collisions, the calculation is multiplied with the nuclear-overlap function T_{AA} for the given event selection [61], assuming an inelastic $p + p$ cross sections of $\sigma_{\rm inel} = 33.8$ mb at 39 GeV $\sigma_{\rm inel} = 35.61$ mb at 62.4 GeV. Table I gives the values. Below 1.5 GeV/c, there is a clear enhancement of the data above the scaled pQCD calculation, consistent with the expectation of a significant thermal contribution.

TABLE I. The values of $T_{\rm AA}$ obtained from Ref. [61].

$\sqrt{s_{NN}}$ (GeV)	Centrality class selection	T_{AA} (mb^{-1})
62.4	0%–20%	18.44 ± 2.49
62.4	20%–40%	6.77 ± 0.82
62.4	0%–86%	6.59 ± 0.89
39	0%–86%	6.76 ± 1.08

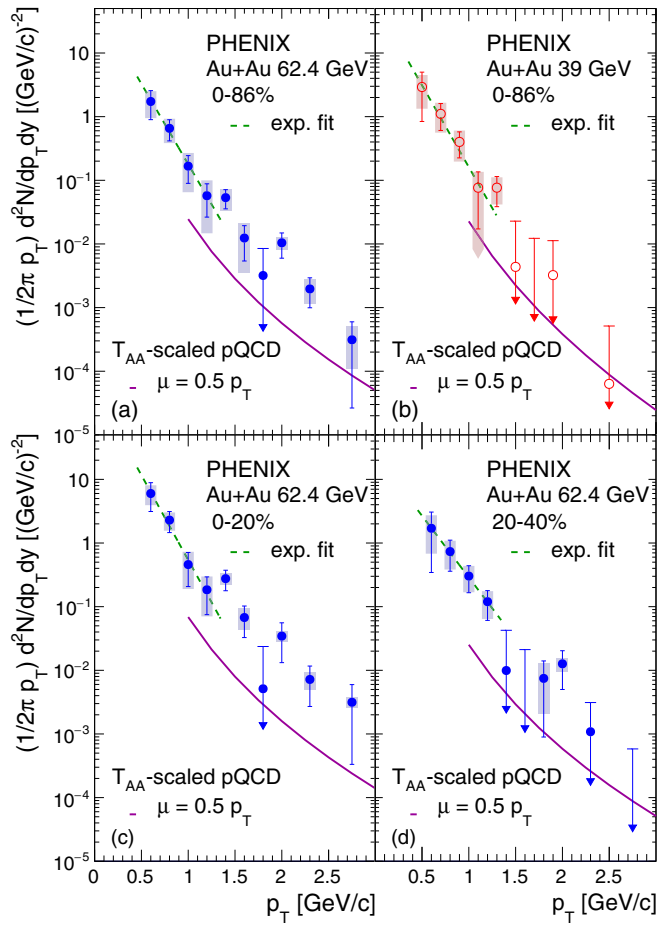

FIG. 9. Direct-photon p_T-spectra in MB (0%–86%) Au+Au collisions at $\sqrt{s_{NN}}$ = (a) 62.4 and (b) 39 GeV. Also shown for 62.4 GeV are the centrality bins (c) 0%–20% and (d) 20%–40%. Data points are shown with statistical (bar) and systematic (box) uncertainties, unless the central value is negative (arrows) or is consistent with zero within the statistical uncertainties (arrows with data point). In these cases the upper limits are given with confidence levels of 95%.

To characterize the enhancement, the data is fitted with a falling exponential function given by

$$\frac{1}{2\pi}\frac{d^2N}{dp_T dy} \approx \exp\left(-\frac{p_T}{T_{\rm eff}}\right). \tag{6}$$

The data sets were fitted below a p_T of 1.3 GeV/c, where statistics are sufficient. Table II summarizes the results, which are also shown in Fig. 9. Systematic uncertainties were obtained with the conservative assumption that the uncertainties are anticorrelated over the observed p_T range. All values are consistent with a common inverse slope $T_{\rm eff}$ of ≈0.170 GeV/c. For the MB and 0%–20% centrality Au+Au sample at 62.4 GeV, the data in the range from 0.9 to 2.1 GeV/c is also fitted. The values are slightly above 0.24 GeV/c and are larger than the value extracted for the lower-p_T range. A possible increase of $T_{\rm eff}$ with p_T is consistent with the values obtained from Au+Au at 200 GeV [35] and Pb+Pb at 2.76 TeV [39], which were fitted in the higher-p_T range. See a more detailed discussion in the next section.

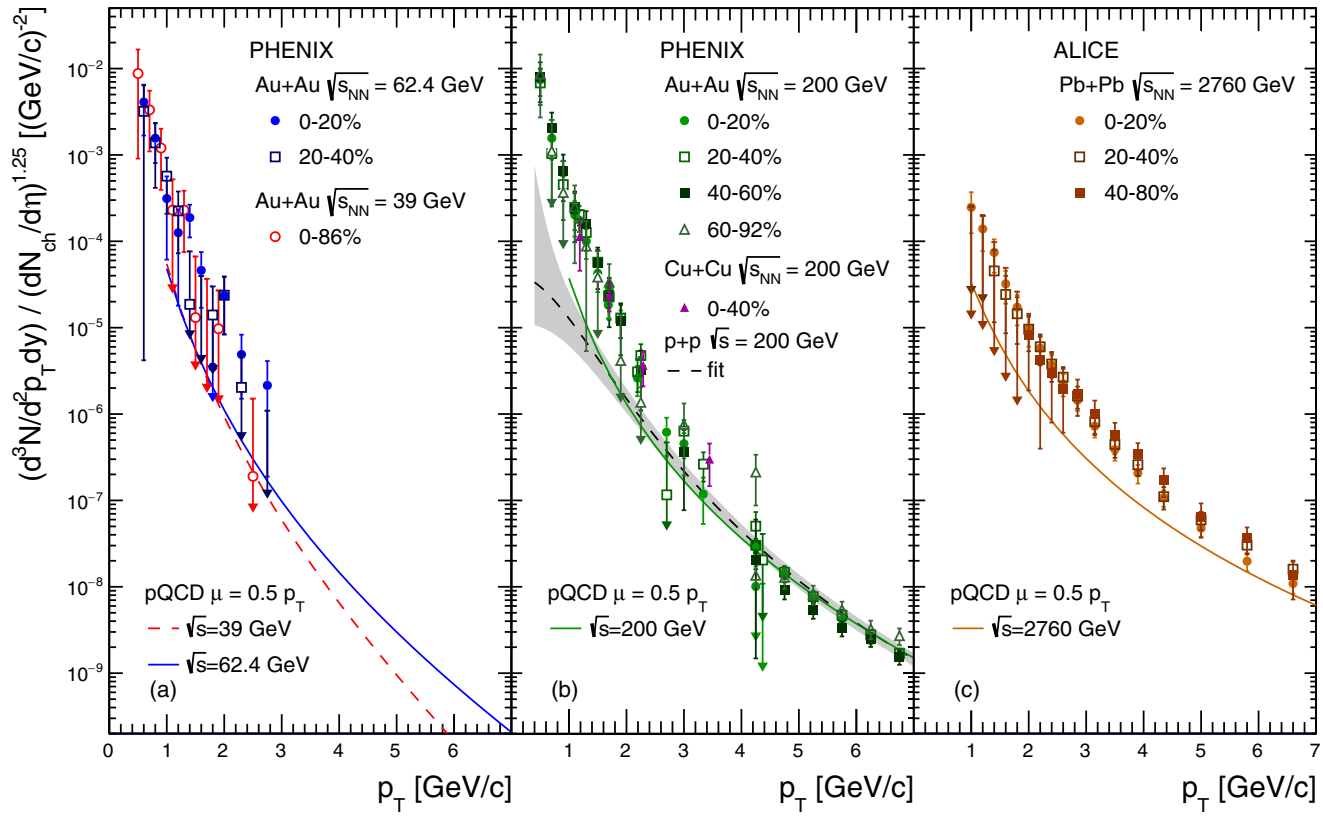

FIG. 10. Direct-photon p_T-spectra normalized by $(dN_{\rm ch}/d\eta)^{1.25}$ for (a) the MB Au+Au 39 and centrality selected 62.4 GeV data sets from Fig. 9, (b) various centrality selected 200 GeV Au+Au [34,35,41] and Cu+Cu [47] data sets, and (c) various centrality selected Pb+Pb 2760 GeV data sets [39]. Also shown in (c) is the $p+p$ fit discussed in the text. The pQCD curves in the three panels are from Refs. [10,60]. The error bars shown are total uncertainties, i.e., the quadrature sum of statistical and systematic uncertainties.

III. COMPARISON TO DIRECT-PHOTON MEASUREMENTS FROM HIGHER COLLISION ENERGIES

In this section, the direct-photon results from Au+Au collisions at 39 and 62.4 GeV are discussed in the context of other direct-photon measurements from heavy ion collisions at higher collision energies, specifically Au+Au collisions at 200 GeV from RHIC and Pb+Pb collisions at 2.76 TeV from LHC. The discussion is divided into three parts. The first part recalls the already published scaling behavior of the direct photon yield with $(dN_{\rm ch}/d\eta)^{\alpha}$ [40]. The next part takes a closer look at the p_T and $\sqrt{s_{NN}}$ dependence of the inverse slope $T_{\rm eff}$ of the direct-photon p_T spectra. The last part investigates the dependence or independence of the scaling variable α on the p_T range.

TABLE II. Inverse slopes fitted to the direct-photon spectra in different p_T ranges.

p_T (GeV/c)	$\sqrt{s_{NN}}$ (GeV)	Centrality class	$T_{\rm eff}$ (GeV/c)	χ^2/NDF
$p_T < 1.3$	62.4	0%–20%	$0.163 \pm 0.031 \pm^{0.016}_{0.009}$	0.44/2
	62.4	20%–40%	$0.224 \pm 0.067 \pm^{0.034}_{0.018}$	0.01/2
	62.4	0%–86%	$0.172 \pm 0.032 \pm^{0.022}_{0.011}$	0.16/2
	39	0%–86%	$0.169 \pm 0.035 \pm^{0.020}_{0.011}$	0.41/2
$0.9 < p_T < 2.1$	62.4	0%–20%	$0.241 \pm 0.048 \pm^{0.024}_{0.012}$	6.96/4
	62.4	0%–86%	$0.245 \pm 0.046 \pm^{0.044}_{0.016}$	5.61/4

A. Scaling of the direct-photon yield with $(dN_{\rm ch}/d\eta)^{\alpha}$

It was shown in Ref. [40] that the direct-photon yield from heavy ion collisions is approximately proportional to $(dN_{\rm ch}/d\eta)^{\alpha}$ with common power $\alpha \approx 1.25$ across collision energies, systems, and centrality. Figure 10 presents the direct-photon yield normalized to $(dN_{\rm ch}/d\eta)^{1.25}$ for a large range of data sets.[6] Panel (a) shows the data sets that are derived from the Au+Au measurements at 39 and 62.4 GeV shown in Fig. 9. Panel (b) presents PHENIX measurements

[6]The WA98 data are not shown here and in the following plots. The upper limits from WA98 for p_T <1.5 GeV/c are consistent with the lower end of the uncertainties of the PHENIX 62.4 GeV and 39 GeV data, but they do not significantly constrain the scaling behavior at low p_T. The STAR data are also not shown as the tension with the PHENIX data remains unresolved, while the multiple publications from PHENIX, based on different data sets and analysis methods, show self consistent results. If taken at face value, the STAR data do demonstrate a similar scaling behavior with $N_{\rm ch}$ for p_T <2 GeV/c, but at a factor-3-lower direct-photon yield.

TABLE III. Values for $dN_{\rm ch}/d\eta$ and $N_{\rm coll}$ obtained from published experimental data. The collaboration and reference numbers are indicated in column six. See text for explanation of the extrapolation used for the $p+p$ collision data at 62.4 GeV. The same $dN_{\rm ch}/d\eta$ and $N_{\rm coll}$ were used for the corresponding pQCD curves in Figs. 10 and 13–15.

Collision system	$\sqrt{s_{NN}}$ (GeV)	Centrality class	$dN_{\rm ch}/d\eta$	$N_{\rm coll}$	Collaboration [Ref.]
$p+p$	62.4	–	1.86 ± 0.08	1	UA5 [62–64]
	200	–	2.38 ± 0.17	1	PHENIX [61]
	2760	–	3.75 ± 0.26	1	ALICE [65]
Cu+Cu	200	0%–40%	109.3 ± 7.8	108.2 ± 12.0	PHENIX [61]
	200	0%–94%	51.7 ± 3.6	51.8 ± 5.6	”
Au+Au	39	0%–86%	104.3 ± 8.9	228.4 ± 36.5	PHENIX [61]
	62.4	0%–86%	131.5 ± 11.2	228.5 ± 30.9	”
	62.4	0%–20%	341.2 ± 29.3	656.6 ± 88.7	”
	62.4	20%–40%	151.8 ± 12.7	241.1 ± 29.2	”
	200	0%–20%	519.2 ± 26.3	770.6 ± 79.9	”
	200	20%–40%	225.4 ± 13.2	241.1 ± 28.4	”
	200	40%–60%	85.5 ± 8.0	82.6 ± 9.3	”
	200	60%–92%	16.4 ± 2.8	12.1 ± 3.1	”
Pb+Pb	2760	0%–20%	1206.8 ± 45.8	1210.9 ± 132.5	ALICE [66]
	2760	20%–40%	537.5 ± 19.0	438.4 ± 42.0	”
	2760	40%–80%	130.3 ± 5.3	77.2 ± 18.0	”

from Au+Au [34,35,41] and Cu+Cu [47] collisions at $\sqrt{s_{NN}}$ = 200 GeV. Panel (c) uses the ALICE measurement from Pb+Pb collisions at $\sqrt{s_{NN}} = 2760$ GeV [39]. All panels show pQCD calculations for $p+p$ collisions at the corresponding $\sqrt{s}$, extrapolated to $p_T = 1$ GeV/c at the scale $\mu = 0.5\,p_T$ [10,60].

Table III gives the $dN_{\rm ch}/d\eta$ and $N_{\rm coll}$ values, which are are used to normalize the integrated yields and are obtained from published experimental data. The values for $p+p$ collisions at 62.4 are taken from Fig. 52.1 of Ref. [62], which was interpolated between UA5 data at $\sqrt{s} = 53$ GeV [63] and 200 GeV [64]. The values for $p+p$ and heavy ion collisions from $\sqrt{s_{NN}} = 7.7$ GeV to 200 GeV are from PHENIX [61]; the values for 2760 GeV $p+p$ data are from ALICE [65]; and the values for Pb+Pb collision data at 2760 GeV are also from ALICE [66].

Figure 10(b) also gives a fit to the $p+p$ data at $\sqrt{s} =$ 200 GeV [40,47] with the empirical form

$$\frac{d^3N}{d^2p_T dy} = \frac{A_{pp}}{\left(1 + \left(\frac{p_T}{p_0}\right)^2\right)^n}, \tag{7}$$

where the parameters are $A_{pp} = 1.60 \times 10^{-4}$ (Gev/c)$^{-2}$, $p_0 = 1.45$ Gev/c, and $n = 3.3$. The band represents the uncertainty of the fit.

All three panels in Fig. 10 show that at a given $\sqrt{s_{NN}}$ the normalized direct-photon yield from $A+A$ collisions is independent of the collision centrality. This is true both for low and high p_T. Comparing the yield at p_T below 3–4 GeV/c across panels reveals that the yield is also remarkably independent of $\sqrt{s_{NN}}$. Above p_T of 4 to 5 GeV/c the normalized yield does show the expected $\sqrt{s_{NN}}$ dependence and is described by the pQCD calculations.

In the high-p_T range, hard-scattering processes dominate direct-photon production, and these direct-photon contributions are not altered significantly by final-state effects. Different centrality selections show the same normalized yield, which reflects that empirically $N_{\rm coll} \propto dN_{\rm ch}/d\eta^{1.25}$ [40]. It remains surprising that within uncertainties the same scaling also holds at lower p_T where direct-photon emission should be dominated by thermal radiation from the fireball. In the following sections, the similarity of the low-p_T direct-photon spectra, both in shape and in normalized yield, is analyzed more quantitatively.

B. Direct-photon inverse slope $T_{\rm eff}$

To better reveal the similarity of the low-p_T direct-photon spectra across $\sqrt{s_{NN}}$, the normalized yield from the most-central samples (0%–20%) for Pb+Pb at $\sqrt{s_{NN}} = 2760$ GeV, Au+Au at 200 GeV, and Au+Au at 62.4 GeV are superimposed on Fig. 11(a). Below 2.5 GeV/c, the data agree very well, even though they span almost two orders of magnitude in $\sqrt{s_{NN}}$. As already suggested earlier by exponential fits to the 39 and 62.4 GeV data, the low-p_T direct-photon spectra cannot be described by a single inverse slope, but seem consistent with an inverse slope that increases with p_T. Fitting all data shown in the p_T range $p_T < 1.3$ GeV/c and $0.9 < p_T < 2.1$ GeV/c results in inverse slopes of $T_{\rm eff} =$ 0.174±0.018 GeV/c and 0.289±0.024 GeV/c, respectively. Here, the statistical and systematic uncertainties were added in quadrature in the fitting procedure. The fits are also shown in Fig. 11, where the dashed lines extrapolate the fits over the full p_T range.

Figure 12 compares the inverse slopes from the common fit to the fits of the individual data sets. For $\sqrt{s_{NN}} = 62.4$ GeV, the values are from Table II, for 200 GeV the data [34,35] were fitted in the two p_T ranges, and for 2760 GeV the value published in Ref. [66] is shown. For the lower-p_T range a value for MB collisions at $\sqrt{s_{NN}} = 39$ GeV is also included.

Another way to illustrate the commonality of the spectra is to compare the ratio of the normalized yield divided by

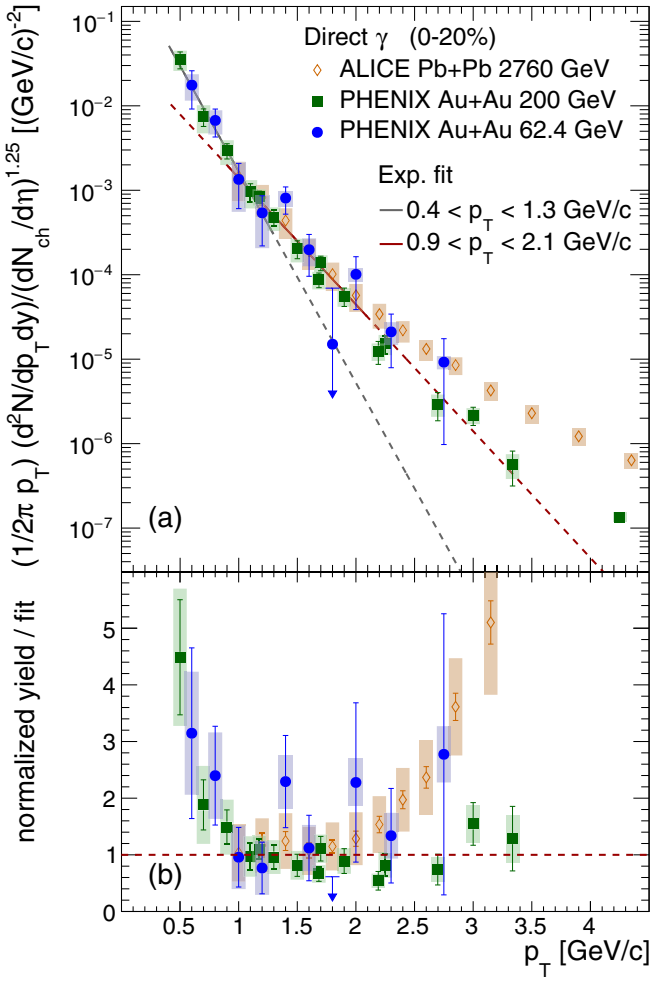

FIG. 11. Direct-photon yield normalized to $(dN_{\rm ch}/d\eta)^{1.25}$ in the low-p_T region for 0%–20% centrality in Pb+Pb at 2760 GeV, Au+Au at 200 GeV, and Au+Au at 62.4 GeV. (a) gives the normalized yield and two exponential fits to the data in the p_T region below 1.3 GeV/c and from 0.9 to 2.1 GeV/c. The dashed line extrapolates the fits beyond the fit ranges. (b) shows the ratio of the data sets to the fit in the range 0.9 to 2.1 GeV/c range.

the extrapolated fit for $0.9 < p_T < 2.1$ GeV/c. The result is shown in Fig. 11(b). Within the uncertainties the ratios are consistent with unity over the fit range for all three $\sqrt{s_{NN}}$. Below 1 GeV/c, where there is no data from $\sqrt{s_{NN}} = 2760$ GeV, the other two energies also agree very well.

The similarity of the spectra in the p_T range up to ≈ 2 GeV/c indicates that the source that emits these photons must be very similar, independent of $\sqrt{s_{NN}}$, a finding that would be consistent with radiation from an expanding and cooling fireball evolving through the transition region from QGP to a hadron gas till kinetic freeze-out. This would naturally occur at the same temperature and similar expansion velocity, independent of the initial conditions created in the collisions.

Above 2 GeV/c, the normalized direct-photon yield becomes $\sqrt{s_{NN}}$ dependent. The $\sqrt{s_{NN}} = 200$ GeV Au+Au data remain consistent with the exponential fit until $p_T \approx 3$ GeV/c,

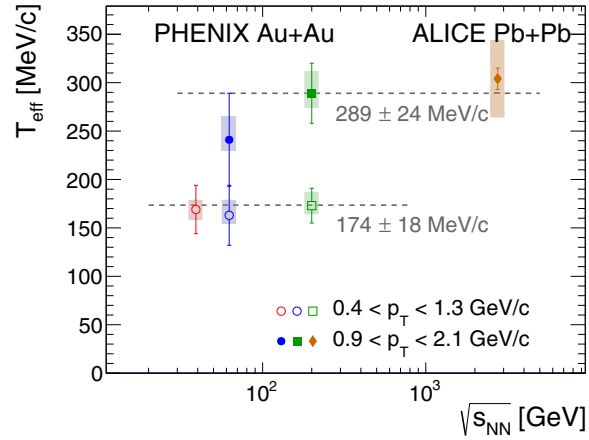

FIG. 12. Inverse slopes, $T_{\rm eff}$, obtained from fitting the combined data from central collisions shown in Fig. 11 is compared to the fit results of the individual data sets at 62.4, 200, and 2760 GeV. Also included is the value for $\sqrt{s_{NN}} = 39$ GeV obtained from fitting the MB data set in the lower-p_T range.

where prompt-photon production from hard-scattering processes starts to dominate (see Fig. 10). In contrast, the Pb+Pb data from $\sqrt{s_{NN}} = 2760$ GeV begin to exceed the exponential $p_T \approx 2$ GeV/c, while prompt-photon production only becomes the main photon source above 4 to 5 GeV/c, where the $N_{\rm coll}$-scaled pQCD calculation describes the heavy ion data well.

This leaves room for additional contributions to the direct-photon spectrum in the range from 2 to 5 GeV/c beyond prompt-photon production, which are $\sqrt{s_{NN}}$ dependent. Such contributions could reflect the increasing initial temperature that would be expected with increasing collision energy.

C. p_T dependence of the scaling variable α

In this final section, the scaling behavior of the direct-photon yield with $(dN_{\rm ch}/d\eta)^{\alpha}$ will be revisited. So far, a fixed value of $\alpha = 1.25$ was used to calculate the normalized inclusive direct-photon yield. This value was obtained from the scaling relation $N_{\rm coll} \propto (dN_{\rm ch}/d\eta)^{\alpha}$ [40]. Here, α will be determined from the direct-photon data itself as a function of p_T. For this purpose, the direct-photon p_T spectra are integrated above a minimum p_T value ($p_{T,\rm min}$) of 0.4 Gev/c, 1.0 Gev/c, 1.5 Gev/c, and 2.0 Gev/c. Panels (a) to (d) of Fig. 13 show the integrated yields as a function of $dN_{\rm ch}/d\eta$ for all data sets shown in Fig. 10. The systematic uncertainties, shown as boxes, give the uncertainty on the integrated yield and the uncertainty on $dN_{\rm ch}/d\eta$. The $A+A$ data are compared to a band representing the integrated yields obtained from the fit to the $p+p$ data at $\sqrt{s} = 200$ GeV, with the functional form given in Eq. (7), scaled by $N_{\rm coll}$. The width of the band is given by the uncertainties on the $p+p$ fit and on $N_{\rm coll}$, combined quadratically. Panels (b) to (c) also show the integrated yields from the $N_{\rm coll}$-scaled pQCD calculations for $\sqrt{s} = 200$ and 2760 GeV.

It is clear from Fig. 10 that all $A+A$ data follow a similar common trend. The PHENIX data in each panel of Fig. 13 is

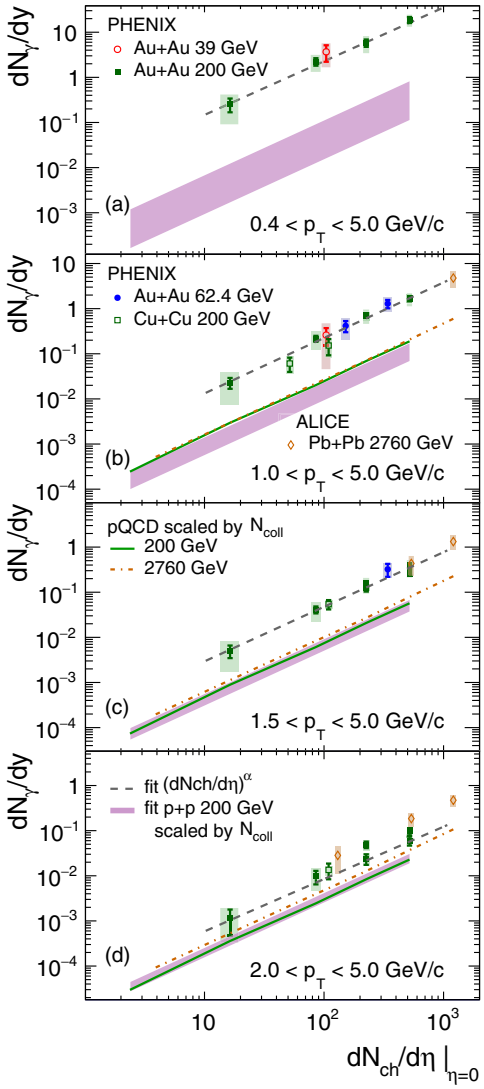

FIG. 13. Integrated invariant direct-photon yields vs. charged particle multiplicity for p_T integrated from (a) 0.4 GeV/c, (b) 1.0 GeV/c, (c) 1.5 GeV/c, and (d) 2.0 to 5.0 GeV/c for all available $A+A$ data sets. The band gives the integrated invariant direct-photon yield from $p+p$ collisions at $\sqrt{s}=200$ GeV, scaled by $N_{\rm coll}$ to the corresponding $dN_{\rm ch}/d\eta$ for the $A+A$ data sets. For (b) to (d) also the scaled and integrated yield from pQCD is given for 200 and 2760 GeV. The dashed lines are the result of fitting the PHENIX data with $A_{\rm ch}(dN_{\rm ch}/d\eta)^{\alpha}$. The fit values for α are consistent with a common value of 1.21±0.04 independent of p_T. Note that the legend for data points, calculations, and fits over (a) to (d) are valid for all panels.

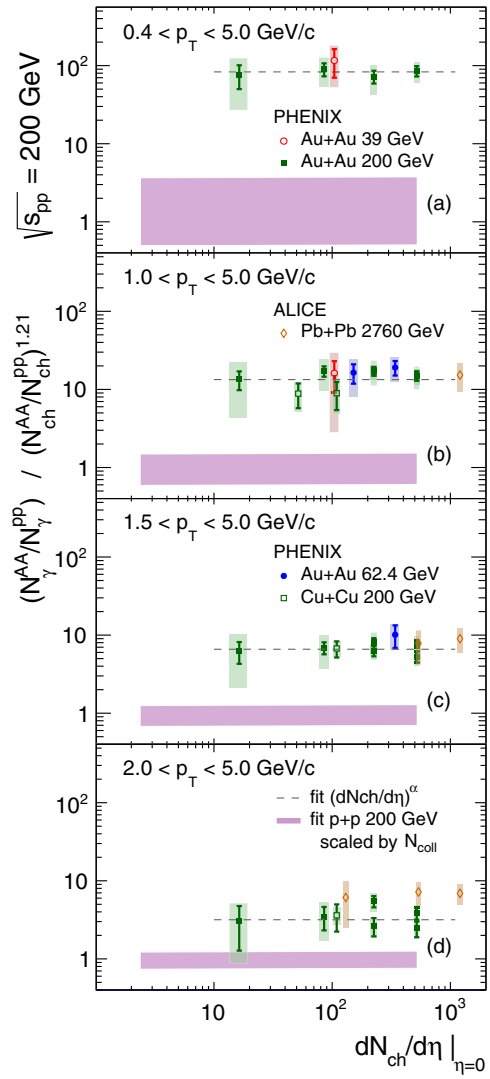

FIG. 14. The ratio of the integrated direct-photon yields from $A+A$ collisions, shown in Fig. 13, to the integrated direct-photon yield from $p+p$ collisions at $\sqrt{s_{NN}}=200$ GeV. The ratio is normalized to the ratio $(dN_{\rm ch}/d\eta^{AA}/dN_{\rm ch}/d\eta^{pp})^{\alpha}$, where $\alpha=1.21$ is the average value from Table IV. (a) to (d) show the different integration regions from (a) 0.4, (b) 1.0, (c) 1.5, and (d) 2.0, to 5.0 GeV/c, respectively. Note that the legend for data points, calculations, and fits that are distributed over (a) to (d) are valid for all panels.

fitted with the scaling relation

$$\int_{p_{T,\rm min}}^{p_{T,\rm max}} \frac{1}{2\pi p_T}\frac{d^2N}{dp_T dy}\,dp_T = A_{\rm ch}\left(\frac{dN_{\rm ch}}{d\eta}\right)^{\alpha}. \qquad (8)$$

The fit results for $p_{T,\rm max}=5$ GeV/c are shown as dashed lines in Fig. 10; the fit parameters are given in Table IV. Here, the dominant systematic uncertainties are due to occupancy dependent differences in the energy scale calibration and on $dN_{\rm ch}/d\eta$. It is assumed that within a given data set these could be anti-correlated and that they are uncorrelated between different data sets. The α values are consistent with an average value of $\alpha=1.21\pm0.04$ (stat), with no evident dependence on $p_{T,\rm min}$. The value is consistent, but slightly lower, than $\alpha=1.25\pm0.02$.

Figure 14 shows the integrated yield from $A+A$ collisions divided by the scaled $p+p$ integrated yield normalized by $((dN_{\rm ch}/d\eta)^{pp}/(dN_{\rm ch}/d\eta)^{AA})^{1.21}$. In this representation, the $p+p$ bands bracket unity with no visible slope. For high p_T the vertical scale would be equivalent to the nuclear-modification factor of prompt photons. For $p_{T,\rm min}=0.4$, 1.0, and 1.5 GeV/c all $A+A$ data have the same absolute value, within statistical and systematic uncertainties, but are

TABLE IV. Fit values obtained from fitting all PHENIX data in panels (a) to (d) in Fig. 13 and (a) and (b) in Fig. 15 with $A_{\rm ch}(dN_{\rm ch}/d\eta)^{\alpha}$. The uncertainties on α are quoted separately as statistical and systematic uncertainties, with the latter including uncertainties from the direct-photon measurements as well as the $dN_{\rm ch}/d\eta$. For the normalization, $A_{\rm ch}$, total uncertainties are given.

$p_{T\,\rm min}$ GeV/c	$p_{T\,\rm max}$ GeV/c	$A_{\rm ch}$	α	χ^2/NDF
0.4	5.0	$(1.06 \pm 0.59) \times 10^{-2}$	$1.19 \pm 0.09 \pm 0.18$	1.18/3
1.0	5.0	$(8.16 \pm 3.46) \times 10^{-4}$	$1.23 \pm 0.06 \pm 0.18$	5.27/8
1.5	5.0	$(1.90 \pm 0.87) \times 10^{-4}$	$1.21 \pm 0.07 \pm 0.16$	6.50/6
2.0	5.0	$(5.55 \pm 3.74) \times 10^{-5}$	$1.16 \pm 0.11 \pm 0.08$	8.85/5
5.0	14.0	$(5.00 \pm 1.08) \times 10^{-7}$	$1.21 \pm 0.02 \pm 0.07$	2.839/7
8.0	14.0	$(7.83 \pm 1.82) \times 10^{-8}$	$1.17 \pm 0.02 \pm 0.06$	2.362/7

significantly enhanced compared to the $p+p$ band. In particular, the Pb+Pb data at $\sqrt{s_{NN}} = 2760$ GeV also shows the same value in panels (b) and (c), even though they were not included in the fit. The enhancement above $p+p$ drops from nearly two orders of magnitude to a factor of ≈ 7 with increasing $p_{\rm T,min}$. In panel (d) for the 2 GeV/c threshold the $\sqrt{s_{NN}} =$ 200 GeV data also have the same value, with an enhancement of $\approx$3. The Pb+Pb data at $\sqrt{s_{NN}} = 2760$ GeV, while also being independent of $dN_{\rm ch}/d\eta$, have a value roughly 30% higher than the 200 GeV data. This illustrates the breakdown of the scaling towards higher p_T, at a p_T for which prompt-photon production is not yet expected to be the dominant source. As can be seen from Fig. 13, in this p_T region the Pb+Pb integrated yield exceeds by a factor of 4 to 5 what is calculated by pQCD for prompt-photon production.

With increasing $p_{\rm T,min}$ the integrated yield becomes increasingly sensitive to the prompt-photon contribution. Integrated direct-photon yields for the ranges $5.0 < p_T < 14$ GeV/c and $8.0 < p_T < 14$ GeV/c are shown in panels (a) and (b) of Fig. 15, together with the corresponding values based on pQCD calculations for the same collision energies. For the integrated yields from Au+Au at 200 GeV, the enhancement compared to $p+p$ has vanished and the measured yield is dominated by prompt-photon production, following closely the scaled and integrated yield calculated by pQCD. Fitting the data with Eq. (8) results in slope values of $\alpha = 1.213 \pm 0.008 \pm 0.070$ and $\alpha = 1.172 \pm 0.016 \pm 0.063$. The full set of fit parameters are given in Table IV. Even though the direct-photon yield is dominated by prompt-photon production the slope values are consistent with those found at lower $p_{\rm T,min}$.

The Pb+Pb data at 2760 GeV continue to be enhanced compared to the pQCD calculations even out to $p_{\rm T,min}$ of 8 GeV/c. The enhancement decreases with $p_{\rm T,min}$ and is $\approx$50% at $p_{\rm T,min} = 5$ GeV/c and reduces to less than 30% for 8 GeV/c. Given the systematic uncertainties on the data and the pQCD calculation these values may already be consistent [39]. Irrespective of whether in addition to prompt-photon production another source is needed to account for the data, the Pb+Pb data can also be well described by a fit with Eq. (8) with $\alpha = 1.12 \pm 0.05$ and 1.21 ± 0.13, for $p_T > 5$ GeV/c and 8 GeV/c, respectively. These values are consistent with values given in Table IV, within the quoted statistical errors.

Figure 16 presents the values of α listed in Table IV, which were obtained from the PHENIX $A+A$ data as function of $p_{\rm T,min}$. Also shown in Fig. 16 are α values from similar fits for several other values of $p_{\rm T,min} > 4$ GeV/c to integrated direct-photon yields from Au+Au data at $\sqrt{s_{NN}} = 200$ GeV published in [35]. Within systematic uncertainties, all α values are consistent with an average value of 1.21 for the thresholds below 4 GeV/c, which is shown as a dashed line.

There is no evidence for a dependence of α on $p_{\rm T,min}$.

Figure 16 compares the data to α extracted from theoretical model calculations of direct-photon radiation [67,68]. The model calculation includes prompt-photon production, radiation from the pre-equilibrium phase, and thermal photons emitted during the evolution from QGP to hadron gas to freeze-out. As discussed in the introduction, in general these and similar calculations qualitatively reproduce the large direct-photon yield and the large anisotropy with respect to the reaction plane observed experimentally, but falls short of a simultaneous quantitative description. Similarly, the model calculation shown in Fig. 16 does not fully describe the dependence of α on p_T. In the region where thermal radiation

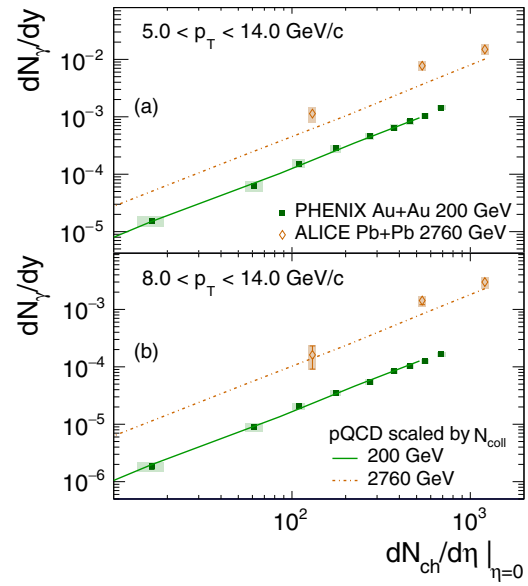

FIG. 15. Integrated direct-photon yields from $A+A$ collisions for $p_{\rm T,min}$ of 5 GeV/c (a) and 8 GeV/c. The representation is the same as in Fig. 13. Also shown are the results from pQCD calculations scaled by $N_{\rm coll}$.

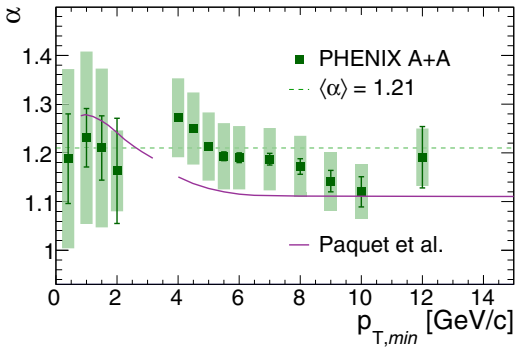

FIG. 16. The α values extracted using fits to integrated direct-photon yields. The dashed line gives the average α value for the four lower $p_{\mathrm{T,min}}$ points. Also shown is a model calculation for α discussed in the text.

is expected to be significant, below $p_T = 2$ GeV/c, the calculated α values are consistent with data, but the calculation predicts a p_T dependence of α which is not seen in the data. In the model calculation, the thermal-photon contribution from the QGP phase depends on $dN_{\mathrm{ch}}/d\eta$ with a higher power of $\alpha \approx 1.8$ than the later stage contribution from the hadron gas $\alpha \approx 1.2$. The $dN_{\mathrm{ch}}/d\eta$ dependence of the prompt contribution is similar to the one from the hadron gas. The dominant sources of direct-photon emission change with increasing p_T from hadron gas to QGP to prompt-photon production, and therefore α would be expected to depend on p_T. While the data do not show such a dependence, the uncertainties, in particular systematic uncertainties, are too large to rule out that α does change with p_T.

IV. SUMMARY

The PHENIX Collaboration presented the measurement of low p_T direct-photon production in MB data samples of Au+Au collisions at 39 and 62.4 GeV recorded at RHIC in 2010. The measurements were performed using the PHENIX central arms to detect photon conversions to e^+e^- pairs in the back plane of the HBD, following the technique outlined in Ref. [35] for the analysis of low-momentum direct photons in Au+Au collisions at 200 GeV. In addition to the MB data samples, the 62.4 GeV/c data was subdivided into two centrality classes, 0%–20% and 20%–40%. For all samples, the relative direct-photon yield, R_γ, was obtained through a double ratio in which many sources of systematic uncertainties cancel. In the p_T range from 0.4 to 3 GeV/c, a clear direct-photon signal is found for all event selections, which significantly exceeds the expectations from prompt-photon production.

The direct-photon p_T spectra are not described by one exponential function, but are consistent with a local inverse slope increasing with p_T. Comparing the 39 and 62.4 GeV data to direct-photon data from Au + Au collisions at $\sqrt{s_{NN}} =$ 200 GeV, also measured by PHENIX, and Pb + Pb collisions at $\sqrt{s_{NN}} = 2760$ GeV, published by ALICE, reveals that the local inverse slopes and the shape of the p_T spectra below 2 Gev/c are independent of $\sqrt{s_{NN}}$ and centrality of the event sample. The combined data for central collisions were fitted with an exponential in the p_T range below 1.3 Gev/c. The inverse slope value found is $T_{\mathrm{eff}} = 0.174 \pm 0.018$ Gev/c. The p_T range from 0.9 to 2.1 Gev/c was also fitted with an exponential function. The inverse slope is significantly larger, with a value of $T_{\mathrm{eff}} = 0.289 \pm 0.024$ Gev/c.

Furthermore, the invariant yield of low-p_T direct photons emitted from heavy ion collisions shows a common scaling behavior with $dN_{\mathrm{ch}}/d\eta$ that takes the form $A_{\mathrm{ch}}(dN_{\mathrm{ch}}/d\eta)^\alpha$. Up to p_T of 2 to 2.5 GeV/c both parameters A_{ch} and α are independent of $\sqrt{s_{NN}}$ and centrality of the event sample. The parameter A_{ch} depends on p_T, but α does not. To extend these observations, the Au+Au data at $\sqrt{s_{NN}} = 200$ GeV and the Pb+Pb data at 2760 GeV were analyzed at larger p_T. It was found that A_{ch} does depend on $\sqrt{s_{NN}}$ even in the p_T range from 2 to 5 GeV/c where direct-photon emission is not yet dominated by prompt-photon production. However, α remains remarkably insensitive to p_T, $\sqrt{s_{NN}}$, and centrality.

A possible scenario, consistent with the observations, is that direct-photon radiation at low p_T originates from thermal processes while the collision system transitions from the QGP phase to a hadron gas. This would naturally be at similar temperature and expansion velocity independent of $\sqrt{s_{NN}}$, collision centrality, and colliding species. In the range from 2 to 5 GeV/c there might be a contribution from the QGP phase earlier in the collision which is more pronounced at higher collision energies. While the data seem qualitatively consistent with this conjecture, model calculations suggest that the $dN_{\mathrm{ch}}/d\eta$ dependence of the direct-photon yield should vary with p_T, as different photon sources are expected to scale differently with $dN_{\mathrm{ch}}/d\eta$ and would contribute to different p_T regions. In contrast, within the experimental uncertainties, no evidence for such a p_T dependence of α was detected.

ACKNOWLEDGMENTS

We thank the staff of the Collider-Accelerator and Physics Departments at Brookhaven National Laboratory and the staff of the other PHENIX participating institutions for their vital contributions. We also thank J. F. Paquet for many fruitful discussions and sharing additional information. We acknowledge support from the Office of Nuclear Physics in the Office of Science of the Department of Energy, the National Science Foundation, Abilene Christian University Research Council, Research Foundation of SUNY, and Dean of the College of Arts and Sciences, Vanderbilt University (U.S.A), Ministry of Education, Culture, Sports, Science, and Technology and the Japan Society for the Promotion of Science (Japan), Conselho Nacional de Desenvolvimento Científico e Tecnológico and Funda cão de Amparo à Pesquisa do Estado de São Paulo (Brazil), Natural Science Foundation of China (People's Republic of China), Croatian Science Foundation and Ministry of Science and Education (Croatia), Ministry of Education, Youth and Sports (Czech Republic), Centre National de la Recherche Scientifique, Commissariat à l'Énergie Atomique, and Institut National de Physique Nucléaire et de Physique des Particules (France), J. Bolyai Research

Scholarship, EFOP, the New National Excellence Program (ÚNKP), NKFIH, and OTKA (Hungary), Department of Atomic Energy and Department of Science and Technology (India), Israel Science Foundation (Israel), Basic Science Research and SRC(CENuM) Programs through NRF funded by the Ministry of Education and the Ministry of Science and ICT (Korea), Physics Department, Lahore University of Management Sciences (Pakistan), Ministry of Education and Science, Russian Academy of Sciences, Federal Agency of Atomic Energy (Russia), VR and Wallenberg Foundation (Sweden), University of Zambia, the Government of the Republic of Zambia (Zambia), the U.S. Civilian Research and Development Foundation for the Independent States of the Former Soviet Union, the Hungarian American Enterprise Scholarship Fund, the US-Hungarian Fulbright Foundation, and the US-Israel Binational Science Foundation.

[1] P. Stankus, Direct photon production in relativistic heavy-ion collisions, Annu. Rev. Nucl. Part. Sci. **55**, 517 (2005).
[2] G. David, R. Rapp, and Z. Xu, Electromagnetic Probes at RHIC-II, Phys. Rep. **462**, 176 (2008).
[3] O. Linnyk, E. L. Bratkovskaya, and W. Cassing, Effective QCD and transport description of dilepton and photon production in heavy-ion collisions and elementary processes, Prog. Part. Nucl. Phys. **87**, 50 (2016).
[4] G. David, Direct real photons in relativistic heavy ion collisions, Rep. Prog. Phys. **83**, 046301 (2020).
[5] H. van Hees, C. Gale, and R. Rapp, Thermal photons and collective flow at the Relativistic Heavy-Ion Collider, Phys. Rev. C **84**, 054906 (2011).
[6] H. van Hees, M. He, and R. Rapp, Pseudo-critical enhancement of thermal photons in relativistic heavy-ion collisions?, Nucl. Phys. A **933**, 256 (2015).
[7] M. Dion, J.-F. Paquet, B. Schenke, C. Young, S. Jeon, and C. Gale, Viscous photons in relativistic heavy ion collisions, Phys. Rev. C **84**, 064901 (2011).
[8] C. Shen, U. W. Heinz, J.-F. Paquet, and C. Gale, Thermal photons as a quark-gluon plasma thermometer reexamined, Phys. Rev. C **89**, 044910 (2014).
[9] C. Shen, J. F. Paquet, G. S. Denicol, S. Jeon, and C. Gale, Thermal Photon Radiation in High Multiplicity $p+\mathrm{Pb}$ Collisions at the Large Hadron Collider, Phys. Rev. Lett. **116**, 072301 (2016).
[10] J.-F. Paquet, C. Shen, G. S. Denicol, M. Luzum, B. Schenke, S. Jeon, and C. Gale, Production of photons in relativistic heavy-ion collisions, Phys. Rev. C **93**, 044906 (2016).
[11] E. L. Bratkovskaya, S. M. Kiselev, and G. B. Sharkov, Direct photon production from hadronic sources in high-energy heavy-ion collisions, Phys. Rev. C **78**, 034905 (2008).
[12] E. L. Bratkovskaya, Phenomenology of photon and dilepton production in relativistic nuclear collisions, Nucl. Phys. A **931**, 194 (2014).
[13] O. Linnyk, W. Cassing, and E. L. Bratkovskaya, Centrality dependence of the direct photon yield and elliptic flow in heavy-ion collisions at $\sqrt{s_{NN}} = 200$ GeV, Phys. Rev. C **89**, 034908 (2014).
[14] M. Chiu, T. K. Hemmick, V. Khachatryan, A. Leonidov, J. Liao, and L. McLerran, Production of photons and dileptons in the Glasma, Nucl. Phys. A **900**, 16 (2013).
[15] L. McLerran and B. Schenke, The glasma, photons and the implications of anisotropy, Nucl. Phys. A **929**, 71 (2014).
[16] L. McLerran and B. Schenke, A tale of tails: Photon rates and flow in ultra-relativistic heavy ion collisions, Nucl. Phys. A **946**, 158 (2016).
[17] C. Klein-Bösing and L. McLerran, Geometrical scaling of direct-photon production in hadron collisions from RHIC to the LHC, Phys. Lett. B **734**, 282 (2014).
[18] J. Berges, K. Reygers, N. Tanji, and R. Venugopalan, Parametric estimate of the relative photon yields from the glasma and the quark-gluon plasma in heavy-ion collisions, Phys. Rev. C **95**, 054904 (2017).
[19] V. Khachatryan, B. Schenke, M. Chiu, A. Drees, T. K. Hemmick, and N. Novitzky, Photons from thermalizing matter in heavy ion collisions, Nucl. Phys. A **978**, 123 (2018).
[20] A. Monnai, Thermal photon v_2 with slow quark chemical equilibration, Phys. Rev. C **90**, 021901(R) (2014).
[21] C.-H. Lee and I. Zahed, Electromagnetic radiation in hot QCD matter: Rates, electric conductivity, flavor susceptibility and diffusion, Phys. Rev. C **90**, 025204 (2014).
[22] S. Turbide, R. Rapp, and C. Gale, Hadronic production of thermal photons, Phys. Rev. C **69**, 014903 (2004).
[23] K. Dusling and I. Zahed, Thermal photons from heavy ion collisions: A spectral function approach, Phys. Rev. C **82**, 054909 (2010).
[24] Y.-M. Kim, C.-H. Lee, D. Teaney, and I. Zahed, Direct photon elliptic flow at energies available at the BNL Relativistic Heavy Ion Collider and the CERN Large Hadron Collider, Phys. Rev. C **96**, 015201 (2017).
[25] M. Heffernan, P. Hohler, and R. Rapp, Universal parametrization of thermal photon rates in hadronic matter, Phys. Rev. C **91**, 027902 (2015).
[26] O. Linnyk, V. Konchakovski, T. Steinert, W. Cassing, and E. L. Bratkovskaya, Hadronic and partonic sources of direct photons in relativistic heavy-ion collisions, Phys. Rev. C **92**, 054914 (2015).
[27] G. Basar, D. E. Kharzeev, and V. Skokov, Conformal Anomaly as a Source of Soft Photons in Heavy Ion Collisions, Phys. Rev. Lett. **109**, 202303 (2012).
[28] G. Başar, D. E. Kharzeev, and E. V. Shuryak, Magneto-sonoluminescence and its signatures in photon and dilepton production in relativistic heavy ion collisions, Phys. Rev. C **90**, 014905 (2014).
[29] B. Müller, S.-Y. Wu, and D.-L. Yang, Elliptic flow from thermal photons with magnetic field in holography, Phys. Rev. D **89**, 026013 (2014).
[30] A. Ayala, P. Mercado, and C. Villavicencio, Magnetic catalysis of a finite size pion condensate, Phys. Rev. C **95**, 014904 (2017).
[31] S. S. Adler *et al.* (PHENIX Collaboration), Centrality Dependence of Direct Photon Production in $\sqrt{s_{NN}} = 200$ GeV Au + Au Collisions, Phys. Rev. Lett. **94**, 232301 (2005).
[32] M. M. Aggarwal *et al.* (WA98 Collaboration), Observation of Direct Photons in Central 158-A-GeV Pb-208 + Pb-208 Collisions, Phys. Rev. Lett. **85**, 3595 (2000).
[33] M. M. Aggarwal *et al.* (WA98 Collaboration), Interferometry of Direct Photons in Central Pb-208+Pb-208 Collisions at 158-A-GeV, Phys. Rev. Lett. **93**, 022301 (2004).

[34] A. Adare *et al.* (PHENIX Collaboration), Enhanced Production of Direct Photons in Au+Au Collisions at $\sqrt{s_{NN}} = 200$ GeV and Implications for the Initial Temperature, Phys. Rev. Lett. **104**, 132301 (2010).

[35] A. Adare *et al.* (PHENIX Collaboration), Centrality dependence of low-momentum direct-photon production in Au + Au collisions at $\sqrt{s_{NN}} = 200$ GeV, Phys. Rev. C **91**, 064904 (2015).

[36] A. Adare *et al.* (PHENIX Collaboration), Observation of Direct-Photon Collective Flow in $\sqrt{s_{NN}} = 200$ GeV Au+Au Collisions, Phys. Rev. Lett. **109**, 122302 (2012).

[37] A. Adare *et al.* (PHENIX Collaboration), Azimuthally anisotropic emission of low-momentum direct photons in Au + Au collisions at $\sqrt{s_{NN}} = 200$ GeV, Phys. Rev. C **94**, 064901 (2016).

[38] L. Adamczyk *et al.* (STAR Collaboration), Direct virtual photon production in Au+Au collisions at $\sqrt{s_{NN}} = 200$ GeV, Phys. Lett. B **770**, 451 (2017).

[39] J. Adam *et al.* (ALICE Collaboration), Direct photon production in Pb-Pb collisions at $\sqrt{s_{NN}} = 2.76$ TeV, Phys. Lett. B **754**, 235 (2016).

[40] A. Adare *et al.* (PHENIX Collaboration), Beam Energy and Centrality Dependence of Direct-Photon Emission from Ultrarelativistic Heavy-Ion Collisions, Phys. Rev. Lett. **123**, 022301 (2019).

[41] S. Afanasiev *et al.* (PHENIX Collaboration), Measurement of Direct Photons in Au+Au Collisions at $\sqrt{s_{NN}} = 200$ GeV, Phys. Rev. Lett. **109**, 152302 (2012).

[42] A. Adare *et al.* (PHENIX Collaboration), Direct photon production in d + Au collisions at $\sqrt{s_{NN}} = 200$ GeV, Phys. Rev. C **87**, 054907 (2013).

[43] A. Adare *et al.* (PHENIX Collaboration), Direct-photon production in $p + p$ collisions at $\sqrt{s} = 200$ GeV at midrapidity, Phys. Rev. D **86**, 072008 (2012).

[44] S. S. Adler *et al.* (PHENIX Collaboration), Measurement of Direct Photon Production in $p + p$ Collisions at $\sqrt{s} = 200$, Phys. Rev. Lett. **98**, 012002 (2007).

[45] V. Khachatryan (PHENIX Collaboration), PHENIX measurements of low momentum direct photon radiation, Nucl. Phys. A **982**, 763 (2019).

[46] A. Drees (PHENIX Collaboration), PHENIX measurements of beam energy dependence of direct photon emission, Proc. Sci. **HardProbes2018**, 176 (2019).

[47] A. Adare *et al.* (PHENIX Collaboration), Low-momentum direct photon measurement in Cu + Cu collisions at $\sqrt{s_{NN}} =$ 200 GeV, Phys. Rev. C **98**, 054902 (2018).

[48] K. Adcox *et al.* (PHENIX Collaboration), PHENIX detector overview, Nucl. Instrum. Methods Phys. Res. A **499**, 469 (2003).

[49] V. Khachatryan, The quark gluon plasma probed by low momentum direct photons in Au+Au collisions at 62.4 GeV and 39 GeV beam energies, Ph.D. thesis, Stony Brook University (2017), https://inspirehep.net/literature/1804505.

[50] A. Adare *et al.* (PHENIX Collaboration), Detailed measurement of the e^+e^- pair continuum in $p + p$ and Au + Au collisions at $\sqrt{s_{NN}} = 200$ GeV and implications for direct-photon production, Phys. Rev. C **81**, 034911 (2010).

[51] M. Allen *et al.* (PHENIX Collaboration), PHENIX inner detectors, Nucl. Instrum. Methods Phys. Res. A **499**, 549 (2003).

[52] K. Adcox *et al.* (PHENIX Collaboration), PHENIX central arm tracking detectors, Nucl. Instrum. Methods Phys. Res. A **499**, 489 (2003).

[53] M. Aizawa *et al.* (PHENIX Collaboration), PHENIX central arm particle ID detectors, Nucl. Instrum. Methods Phys. Res. A **499**, 508 (2003).

[54] L. Aphecetche *et al.* (PHENIX Collaboration), PHENIX calorimeter, Nucl. Instrum. Methods Phys. Res. A **499**, 521 (2003).

[55] W. Anderson *et al.*, Design, construction, operation and performance of a hadron blind detector for the PHENIX experiment, Nucl. Instrum. Methods Phys. Res. A **646**, 35 (2011).

[56] A. Adare *et al.* (PHENIX Collaboration), Evolution of π^0 Suppression in Au+Au Collisions from $\sqrt{s_{NN}} = 39$ to 200 GeV, Phys. Rev. Lett. **109**, 152301 (2012); [**125**, 049901(E) (2020)].

[57] B. I. Abelev *et al.* (STAR Collaboration), Energy dependence of $\pi^{\pm}$, p and anti-p transverse momentum spectra for Au + Au collisions at $\sqrt{s_{NN}} = 62.4$ and 200 GeV, Phys. Lett. B **655**, 104 (2007).

[58] L. Adamczyk *et al.* (STAR Collaboration), Bulk properties of the medium produced in relativistic heavy-ion collisions from the beam energy scan program, Phys. Rev. C **96**, 044904 (2017).

[59] Y. Ren and A. Drees, Examination of the universal behavior of the η-to-π^0 ratio in heavy-ion collisions, Phys. Rev. C **104**, 054902 (2021).

[60] J. F. Paquet, (2017), private communication, uses nuclear PDF nCTEQ15-np and photon fragmentation function BFG-II.

[61] A. Adare *et al.* (PHENIX Collaboration), Transverse energy production and charged-particle multiplicity at midrapidity in various systems from $\sqrt{s_{NN}} = 7.7$ to 200 GeV, Phys. Rev. C **93**, 024901 (2016).

[62] P. A. Zyla *et al.* (Particle Data Group), Review of particle physics, Prog. Theor. Exp. Phys. **2020**, 083C01 (2020).

[63] K. Alpgard *et al.* (UA5 Collaboration), Comparison of $p\bar{p}$ and pp interactions at $\sqrt{s} = 53$ GeV, Phys. Lett. B **112**, 183 (1982).

[64] G. J. Alner *et al.* (UA5 Collaboration), Scaling of pseudorapidity distributions at c.m. energies up to 0.9 TeV, Z. Phys. C **33**, 1 (1986).

[65] J. Adam *et al.* (ALICE Collaboration), Charged-particle multiplicities in proton-proton collisions at $\sqrt{s} = 0.9$ to 8 TeV, Eur. Phys. J. C **77**, 33 (2017).

[66] K. Aamodt *et al.* (ALICE Collaboration), Centrality Dependence of the Charged-Particle Multiplicity Density at Mid-Rapidity in Pb-Pb Collisions at $\sqrt{s_{NN}} = 2.76$ TeV, Phys. Rev. Lett. **106**, 032301 (2011).

[67] J. F. Paquet, (2020), private communication.

[68] C. Gale, J.-F. Paquet, B. Schenke, and C. Shen, Probing early-time dynamics and quark-gluon plasma transport properties with photons and hadrons, Nucl. Phys. A **1005**, 121863 (2021).